The world's second-largest, recorded landslide event: lessons learnt from the landslides triggered during and after the 2018 M_w 7.5 Papua New Guinea earthquake

Hakan Tanyaş[1], Kevin Hill[2], Luke Mahoney[2,3], Islam Fadel[1], Luigi Lombardo[1]

[1]University of Twente, Faculty of Geo-Information Science and Earth Observation (ITC), Enschede, Netherlands

[2]School of Earth Sciences, University of Melbourne, Melbourne, VIC, Australia

[3]Papuan Oil Search Ltd, Sydney, NSW, Australia

Corresponding author: Hakan Tanyaş (h.tanyas@utwente.nl)

Abstract

Widespread landslide events provide rare but valuable opportunities to investigate the spatial and size distributions of landslides in relation to seismic, climatic, geological and morphological factors. This study presents a unique event inventory for the co-seismic landslides induced by the February 25, 2018 M_w 7.5 Papua New Guinea earthquake as well as its post-seismic counterparts including the landslides triggered by either aftershocks or succeeding rainfall events that occurred between February 26 and March 19. We mapped approximately 11,500 landslides of which more than 10,000 were triggered by the mainshock with a total failed planimetric area of about 145 km^2. Such a large area makes this inventory the world's second-largest recorded landslide event after the 2008 Wenchuan earthquake. Large landslides are abundant throughout the study area located within the remote Papua New Guinea Highlands. Specifically, more than half of the landslide population is larger than 50,000 m^2 and overall, post-seismic landslides are even larger than their co-seismic counterparts. Our analyses indicate that large and widespread landslides were triggered as a result of the compound effects of the strong seismicity, complex geology, steep topography and high rainfall. We statistically show that the 15-day antecedent precipitation, as a predisposing factor, contributes to the spatial distribution of co-seismic landslides. Also, we statistically demonstrate that the cumulative effect of aftershocks is the main factor disturbing steep hillslopes and causing the initiation of very large landslides up to the size of ~5 km^2. Taking aside the role of the intense seismic swarm and antecedent precipitation, these inventories also provide evidence for landslide events where the active tectonics contribute to weaken hillslopes and the fatigue damage. Overall, the dataset and the findings provided by this paper is a step forward in seismic landslide hazard assessment of the entire Papua New Guinea mainland.

Keywords: Landslides; earthquakes; antecedent precipitation; discontinuity surfaces; geology; aftershocks; active tectonics; fatigue damage.

1 Introduction

The island of New Guinea lies along the northern margin of the Australian continent and is part of the 'Ring of Fire' around the Pacific Ocean (Figure 1a). As such there are active volcanoes, major earthquakes and many associated landslides (Greenbaum et al., 1995), particularly within the precipitous topography of the Papuan Fold and Thrust Belt (Figure 1b & c).

Papua New Guinea (PNG) comprises the eastern half of the island of New Guinea and has a population of almost 9 million with the second lowest urban population in the world (CIA, 2018) including many subsistence farmers living in the Highlands. The Highlands is also the site of one of the world's richest gold mines at Porgera and major gas and oil production facilities at Hides and Kutubu, with 300 km pipelines to the coast. Therefore, the landslides can be devastating to the local people and facilities.

In the Highlands of central PNG a major earthquake (Mw 7.5) occurred on February 25 (UTC 17:44:44) 2018 which was the strongest earthquake recorded in this region over the past 100 years (Wang et al., 2020). The area was subsequently hit by four strong aftershocks (with $M_w \geq 6.0$) within 9 days after the mainshock (Figure 1b; USGS 2021). The area was highly susceptible to landslides because of climatic, geologic, and tectonic factors (Greenbaum et al., 1995; Robbins and Petterson, 2015) and due to amplification of seismic shaking by the local environmental conditions. As a result, landslides were reported as the most disastrous hazard related to the 2018 PNG earthquake and described as events "killing and burying people and houses, affecting water sources and destroying crops" (WHO, 2018). Although the earthquakes occurred in a sparsely populated area, they still directly or indirectly affected 544,000 people; of which 270,000 people required immediate humanitarian assistance, and 34,100 people were ultimately displaced (WHO, 2018).

The USGS Ground Failure tool estimated approximately 500 km^2 of area exposed to landslide hazard associated with this earthquake (Allstadt et al., 2016; Nowicki Jessee et al., 2018). To help mitigate the effects of future landslides induced by earthquakes it is essential to analyze the landslides resulting from the 2018 earthquakes and generate an earthquake-induced landslide (EQIL) inventory. This constitutes the first step towards generating a landslide hazard map which can be used to make future habitation safe and allow further safe construction and development. Additionally, new understandings related to this landslide event could be valuable to improve the existing predictive methods developed for EQILs (e.g., Robinson et al., 2017; Nowicki Jessee et al., 2018; Tanyaş et al., 2019a; Lombardo et al., 2021). Here we produce an EQIL inventory for the 2018 earthquakes leading towards those advanced hazard assessment products.

1.1 Tectonic and geological setting

The island of New Guinea comprises the northern margin of the Australian continent (Figure 1a) and is politically divided into the West Papuan province of Indonesia in the west and Papua New Guinea (PNG) in the east (Figure 1b). The north-south oriented political border roughly coincides with the Tasman Line (Scheibner, 1974) separating Proterozoic basement to the west from accreted Palaeozoic terranes to the east (Figure 1c & d; Hill and Hall, 2003). The reader is referred to Hill & Hall (2003) for a comprehensive discussion of the structure and tectonics of the New Guinea region.

Tectonically the island is divided into four main belts following Tertiary arc-continent collisions (Hill and Hall, 2003; Mahoney et al., 2019). In the south, the Stable Platform is the northward continuation of the Australian continent (Figure 1a) which has been relatively undeformed since the Jurassic (Figure 1b-d). To the north-northeast of the Stable Platform is the Fold Belt which comprises deformed Mesozoic and Tertiary sediments that overlie crustal-scale normal faults in basement many of which have been inverted (Figure 1d). The deformation commenced in the Mid-Late Miocene to Pliocene and continues today. The leading edge of the Fold Belt is seismically active and represents a major plate-boundary fault-zone between the Australian and Pacific Plates (Abers and McCaffrey, 1988; Mahoney et al., 2021; Pegler et al., 1995; Wallace et al., 2004). Further north-northest lies the Mobile Belt (Figures 1b-d) which comprises igneous, metamorphic and ophiolitic rocks that are intensely deformed by strike-slip and compressive stresses. Along the north coast is the fragmented arc that accreted to the margin in the Late Miocene causing the orogenesis. The Mobile Belt and Accreted Arc overlie a north- and south- dipping subduction zone (Figure 1d) that plunges to the west beneath West Papua and which is well defined by earthquake foci in Figure 1b (e.g., Pegler et al., 1995).

Within the Papuan Fold and Thrust Belt (PFTB) in PNG, the most abundant outcropping geological units are the Oligocene-Miocene Darai Limestone and the overlying syn-orogenic sequences (e.g., Figure 1e). In the NE of the PFTB, the Darai Limestone grades into the volcaniclastic sediments of the Aure Beds derived from a volcanic arc in the Mobile Belt that overlies the south-dipping subduction zone (Figure 1d) (Hill et al., 1990). Following the onset of compression at ~14-12 Ma (Hill and Raza, 1999) the volcanics and volcaniclastics prograded south depositing the Older volcanics or Wongop Molasse. These beds interfinger with the upper Darai Limestone and Orubadi Beds. As the PFTB propagated south in the Pliocene, the Darai, Orubadi and Wongop beds were folded, thrusted, uplifted and eroded to make the precipitous present-day topography (Figure 1b). In the last 0.5 Ma large strato-volcanoes developed within the PFTB, predominantly focused along pre-existing NE-SW lineaments in basement (Hill et al., 2002). These volcanoes and the volcanoclastic rocks derived from them (e.g., Kagua Clays and other Quaternary beds) comprise the Newer volcanics and are largely undeformed.

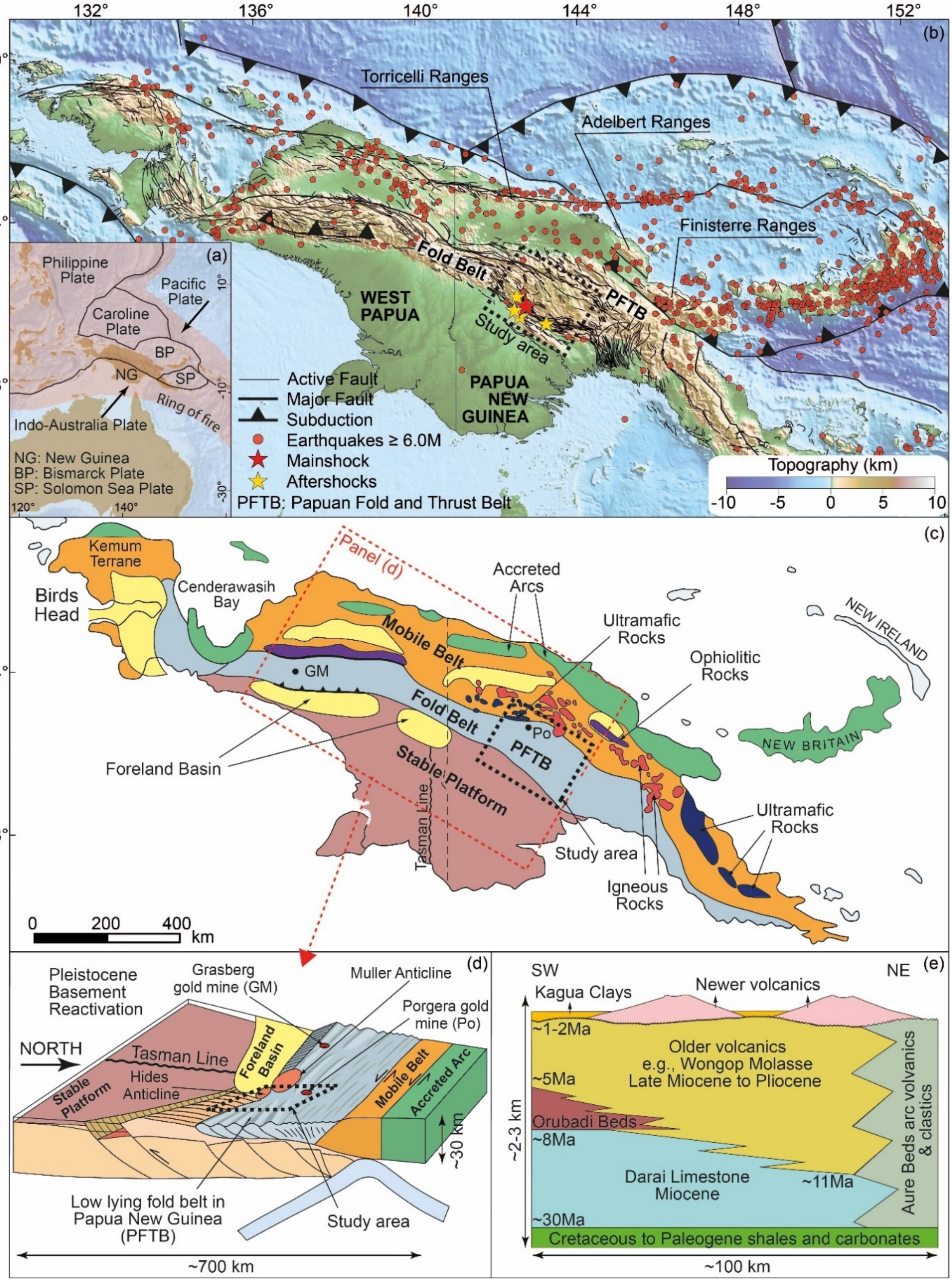

Figure 1. Location, tectonic setting and stratigraphy of PNG. (a) The location of the area along the tectonically active boundary between the Australian and Pacific plates. (b) Physiography, tectonic boundaries (Pegler et al., 1995) and historical earthquakes in New Guinea (USGS 2021). (c) Simplified tectonic belts and the principal tectonic features of New Guinea (after Hill & Hall 2003). (d) 3D sketch of the main tectonic divisions and structures in New Guinea, looking west. The fold and thrust belt is shaded light blue. (e) Stratigraphic relationships in the Neogene to Recent section in the study area (after Mahoney et al., 2017).

1.2 2018 PNG earthquake characteristics

The M_w 7.5 PNG Highlands earthquake occurred on February 25 within the PFTB, which is characterized by steep and deformed hillslopes exposed to intense precipitation through the year (e.g., Mahoney et al., 2017). It occurred at a depth of between 15-30 km beneath the frontal PFTB structures ~96 km west of Mendi. However, the precise location and depth of the earthquake is associated with significant uncertainty due to the absence of a local seismograph network and because of the remoteness of the event relative to the Global Seismographic Network (GSN) (e.g., Mahoney et al., 2021). The M_w 7.5 mainshock was followed by four aftershocks ≥ Mw 6.0 within 9 days after the mainshock. All four earthquakes ≥ Mw 6.0 occurred at mid-crustal focal depths (~15-30 km) and were associated with reverse offset along NW-SE striking faults (USGS Earthquake Portal; Figure 1b and Figure 2). Finite fault models suggest that multiple faults ruptured during the earthquake sequence, however the reported fault dips vary significantly (e.g., Chong and Huang, 2020; Wang et al., 2020). Co-seismic ground deformation, as indicated by satellite and GPS measurements, extended over 7,500 km^2 and uplift reached up to 1.2 m (Mahoney et al., 2021).

1.3 Background on landslides

Over the past two decades, we have advanced our understanding of co-seismic landslides and their impacts (Fan et al., 2019). Various methods have been proposed to assess the hazardous consequences of co-seismic landslides based on mechanistic (e.g., Jibson et al. 2000; Jibson 2007; Kaynia et al. 2011; Saade et al. 2016; Gallen et al. 2017; Song et al. 2021), statistical (e.g., Kritikos et al. 2015; Robinson et al. 2017; Parker et al. 2017; Nowicki Jessee et al. 2018; Tanyaş et al. 2019a; Lombardo et al. 2021) and empirical methods (e.g., Tanyaş et al. 2019b; Tanyaş and Lombardo 2019). Currently, the U.S. Geological Survey (USGS) Ground Failure tool provides estimates regarding the distribution of co-seismic landslides in near-real-time (Allstadt et al., 2016).

Through this scientific progress, earthquake-induced landslide (EQIL) inventories have provided valuable information helping us to better understand the factors controlling the spatial and size distribution of landslides. Therefore, they significantly contribute to the progress in the rapid assessment of co-seismic landslides (e.g., Wasowski et al., 2011). Specifically, strong earthquakes triggering tens of thousands of landslides receive a lot of attention from the worldwide scientific community (e.g., Harp and Jibson, 1995; Gorum et al., 2011; Roback et al., 2018) and due to the increasing availability of high-resolution imagery, multiple landslide inventories have been recently mapped (Tanyaş et al., 2017). Despite this strong interest in large EQIL-events, as of July 2021, no EQIL inventory or detailed landslide study regarding the 2018 Papua New Guinea (PNG) earthquake (M_w 7.5) has been published.

In PNG, earthquakes are the second-most common triggering factor of landslides after rainfall (Robbins and Petterson, 2015) and three major EQIL-events are reported in the literature, associated with the following earthquake sequences (see Figure 2):

- (i) 1935 Torricelli Mountains (Simonett, 1967; Stanley, 1935),
- (ii) 1970 Adelbert Range (Pain, 1972)
- (iii) 1993 Finisterre Mountains (Meunier et al., 2007).

Among these cases, the Finisterre Mountains earthquake sequence is the only case with an available EQIL inventory (Meunier et al., 2007).

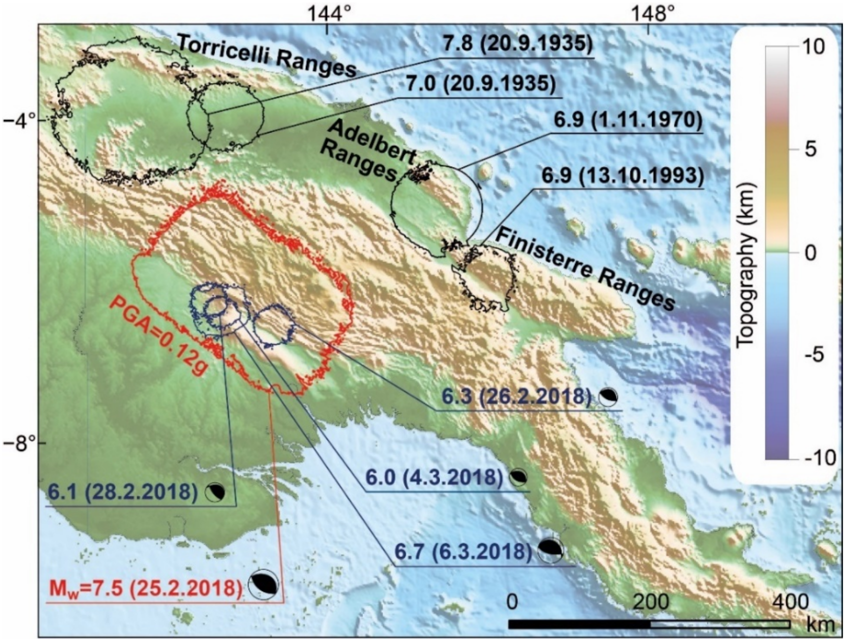

Figure 2. Map showing the estimated largest area affected by documented EQIL-events in PNG. The 0.12 g refers to the global minimum PGA containing at least 90% of the landslides in the EQIL inventories (see Tanyaş and Lombardo, 2019). The red line corresponds to the 0.12g PGA contour of the 2018 PNG earthquake.

The area affected by the 2018 PNG earthquake is much larger than any of the documented EQIL-events (the red polygon in Figure 2). The total area bounded by the peak ground acceleration (PGA) contour of 0.12 g approximately extends over 52,500 km^2 and represents the study area under examination in this work. The PGA contour of 0.12 g (released by the U.S. Geological Survey; ShakeMap, Worden and Wald, 2016) corresponds to the estimated outermost limit encompassing the main landslide-affected area containing at least 90% of the landslides (see Tanyaş and Lombardo, 2019).

Overall, except for a few articles focusing on the fault rupturing mechanism and associated ground deformation (e.g., Chong and Huang, 2020; Mahoney et al., 2021), there is no detailed investigation regarding the failure mechanism, extent, nor spatial distribution of landslides triggered by this unique earthquake sequence. Chong and Huang (2020) indicate that in some locations, the surface subsidence identified by Synthetic Aperture Radar (SAR) images matches with landslides, which were most likely triggered by the earthquake sequence. Also, Mahoney et al (2021) point out the link between surface deformation and co-seismic landslides. Additionally, they provide valuable insight into the mechanism of EQILs, specifically by emphasizing the possible influence of structural features and lithology on the initiation of landslides.

Assessment of structural features or more specifically of discontinuity surfaces such as joints, faults, bedding, and foliation planes as well as the interface between weathered hillslope materials and fresh bedrock is an important component of slope stability analyses (e.g., Stead and Wolter, 2015). However, this requires detailed geotechnical investigation. Although some studies exist reporting or documenting the role of discontinuity surfaces, in particular, for large populations of EQILs (e.g., Chigira et al., 2003; Chigira and Yagi, 2006; Gorum et al., 2011), establishing relationships between the spatial distribution of EQILs and discontinuity surfaces is still a challenge for landslide scientists (Ling and Chigira, 2020).

The existence of discontinuity surfaces is an important factor in terms of slope stability because they do not only introduce weakness planes but also control the distribution of pore water pressure (e.g., Perrone et al., 2008). Discontinuity surfaces have long been recognized as a crucial factor controlling the occurrence of landslides in PNG (Greenbaum et al., 1995; Robbins and Petterson, 2015). In this context, tectonically and geologically inherited features also constitute important controls on hillslope stability by increasing the slope steepness and/or by introducing weakness planes such as lithological variations or fracturing (Korup, 2004; Ambrosi and Crosta, 2006; Dai et al., 2011). Intense active tectonics, as observed in PNG, could introduce progressive deformation and cause large rockslides (e.g., Ambrosi and Crosta, 2006; Penna et al., 2017).

In addition to structural features and active tectonics, rainfall has been reported as the main triggering factor of landslides in PNG (Robbins and Petterson, 2015). This makes the 2018 PNG event that occurred in the tropics more interesting because in the literature, there are only a few EQIL-events that occurred in wet seasons and they all emphasize the importance of rainfall events as a predisposing factor that amplifies the triggering effect of seismicity (e.g., Sassa et al., 2007; Wang et al., 2019). The lack of global observations regarding EQIL-events that occurred during wet seasons hampers our ability to study, understand and consequently model EQIL susceptibility in the context of co-existing precipitation and seismic shaking. For instance, although several global-scale predictive EQIL methods are already available (Kritikos et al., 2015; Nowicki Jessee et al., 2018; Nowicki et al., 2014; Parker et al., 2017; Robinson et al., 2017; Tanyaş et al., 2019a), none of them can account for the antecedent precipitation due to the lack of landslide inventory reflecting such conditions.

This study fits in this framework by presenting multiple EQIL inventories related to the mainshock of the 2018 PNG earthquake as well as the subsequent aftershocks, both taking place under the exposure to rainfall discharge. Landslide populations associated with co-seismic and post-seismic conditions are subsequently examined in terms of their spatial and size distribution in association with the governing slope, rainfall precipitation and tectonic governing parameters.

1.4 Climatic characteristics of the study area

PNG is located in the Maritime Continent and is periodically exposed to the West Pacific Monsoon, which in turn produces a distinct seasonal precipitation cycle (Smith et al., 2013, 2012). Monsoons' dynamics are governed by large differences between the land and the ocean temperatures. In the Maritime Continent, the intensity of the monsoon season is quite variable over time but it is well correlated to the El Niño-Southern Oscillation (McBride et al., 2003; Robertson et al., 2011). The 2018 PNG earthquake occurred during a weak La Niña event (WMO, 2018). This means that 2018 was not a year with severe hurricanes for PNG.

PNG has a characteristic wet season that spans from November to April (Figure 3, Smith et al., 2013). However, different microclimatic conditions exist for the northern and the southern part of Papua Fold and Thrust Belt because of the mountain belt. Based on the 20 years (from 2000-06-01 to 2020-12-31) rainfall time series accessed via the Integrated Multi-Satellite Retrievals Final Run product (IMERG; Huffman et al., 2019), available through Giovanni online data system (v.4.32; Acker and Leptoukh, 2007), the average annual rainfall is 3392 mm for the study area.

Figure 3a shows that monthly average precipitation varies from 175 to 500 mm through the study area. For the whole study area, the total precipitation estimated for February and March 2018 are 258 mm and 316 mm, respectively, which are slightly lower than the monthly average rainfall computed for these months (February, 290 mm and March, 375 mm) over the 20-year time span we considered here (Figure 3b). The time series that we sampled for the Mount Kerewa, Mount Sisa and Mount Bosavi volcanoes, representing the central part of the study area from north to south, show that the wet and dry seasons are consistent in these locations (Figure 3c). However, the long-term trends do not fully match with the precipitation records of 2018 (Figure 3d). For instance, for the Mount Bosavi region, July appears as the wettest month (Figure 3d), although it is the driest one based on the 20-year time series (Figure 3c). Overall, in 2018, monthly precipitation amounts varied from ~80 mm to ~350 mm from the northern to southern part of the area under consideration for February and March 2018 (Figure 3d).

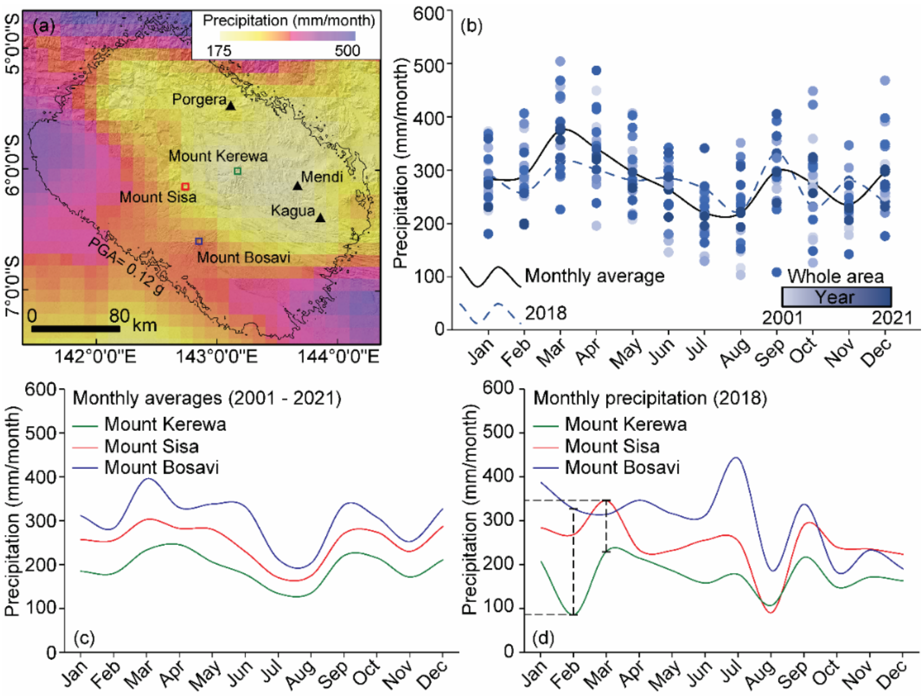

Figure 3. Plots showing (a) monthly average precipitation, (b) variation of the monthly precipitation in the study area delineated by PGA=0.12 g PGA contour, (c) monthly average precipitation for Mount Kerewa, Mount Sisa and Mount Bosavi and (d) monthly precipitation amounts of 2018. The average values were calculated based on the 20-year time series of IMERG Final Run product (Huffman et al., 2019) was used for the plots. In panel (b), each dot corresponds to the monthly rainfall estimated for each of the 20 years under examination.

2 Materials and methods

2.1 Landslide Mapping

To map EQILs, we initially identified the most likely area affected by landslides following the method proposed by Tanyaş and Lombardo (2019). The method identifies the areal coverage of the topographically landslide-prone areas with respect to 0.12 g isoline (i.e., the minimum PGA containing at least 90% of the landslides) and establishes an empirical relationship to predict the area affected by landslides.

We used topographic data to extract the landslide-prone areas. Specifically, we accessed the Shuttle Radar Topography Mission (SRTM) digital elevation model, with 1 arc-second (30 m) spatial resolution (NASA JPL, 2013). We accessed the PGA map of the 2018 PNG earthquake released by the U.S. Geological Survey (USGS) ShakeMap (approximately 1 km spatial resolution, Worden and Wald, 2016). We then masked out flat areas (i.e., slope < 5° and local relief < 100 m) located within the 0.12g isoline and used the relationship proposed by Tanyaş and Lombardo (2019) to predict the EQIL-affected area. Based on this approach, we identified the area encompassed by the 0.26 g isoline as the most likely area affected by landslides, which defined the primary target area to map landslides (Figure 4).

Within this area we identified pre- and post- seismic (i.e., with reference to the mainshock) images suitable to map landslides (Figure 4). The suitability of an image was primarily based on the intensity of cloud cover in the area. We opted for a multi-temporal mapping procedure that involved using multiple satellite scenes providing new information that may have been previously unavailable due to the cloud cover. To support this systematic landslide mapping, we used PlanetScope (3-5 m) and Rapid Eye (5 m) images acquired from Planet Labs (Planet Team, 2017) as well as high-resolution Google Earth scenes. The mapping procedure was then based on visual interpretation. We used both pre- and post- seismic images to identify co-seismic landslides (i.e., landslides triggered by the February 25, 2018 mainshock). We also mapped landslides triggered by subsequent aftershocks and/or rainfall events (i.e., post-seismic landslides).

Overall, we systematically examined an area of 24,305 km^2. The acquisition date of the oldest pre-seismic image is November 25, 2017, which dates back 91 days before the 2018 PNG earthquake. However, 98% of the study area was examined using images acquired within the last 50 days before the earthquake, whereas 60% of images date back to two weeks before the earthquake at most (Figure 4). As a result, we believe that we have excluded most pre-existing landslides from our EQIL inventory.

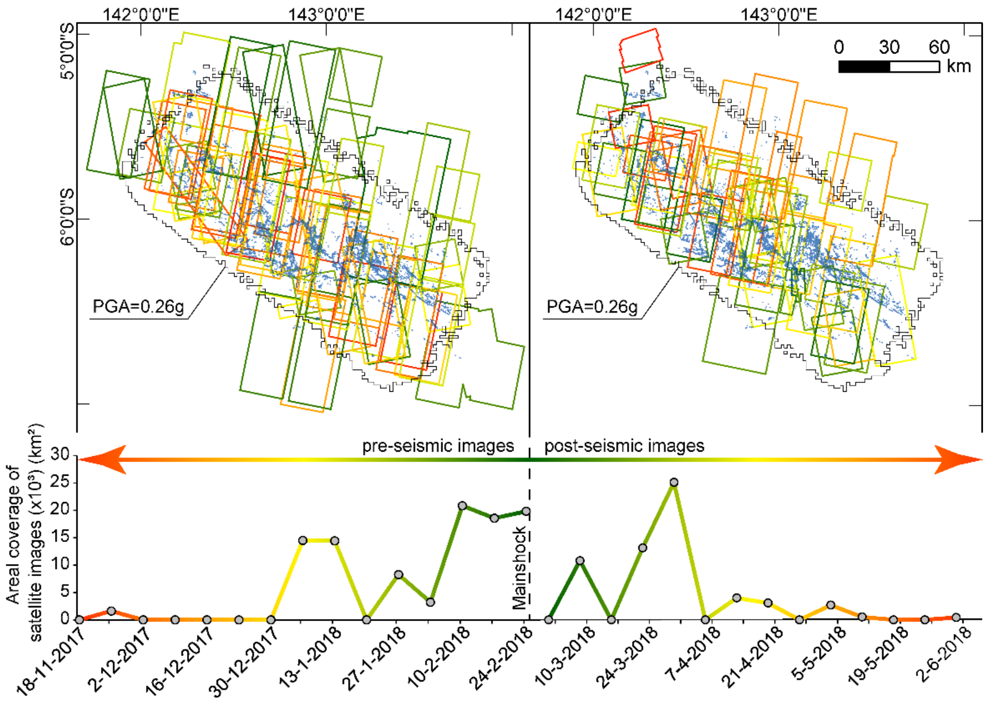

Figure 4. Boundaries and spatial distributions of the examined pre- and post- seismic images and their acquisition dates.

As for the post-seismic period, 82% of the images used for mapping were acquired within a month after the earthquake (Figure 4), over which period the area was hit by four strong aftershocks (M_w≥6.0). Therefore, differentiating landslides triggered by the mainshock or by the aftershocks was a challenge. To address this issue, we used images acquired soon after the earthquake to confirm if they were triggered by the mainshock, even if it was not possible to delineate the landslide boundaries precisely due to the cloud cover. We demonstrate our iterative approach in Figure 5. The top left panel reports the situation prior to the mainshock (Figure 5a). The first set of available images following the mainshock were acquired on February 26, which is just a day after the mainshock. This imagery is shown in Figure 5b where a large number of landslides were triggered by ground motion although could not be clearly mapped due to the cloud cover. To complete this information, we kept on examining subsequent scenes and found a clearer image just nine days later. This is shown in Figure 5c where many other landslides could be mapped in addition to those seen in panel (b) but a few areas were still masked by clouds. To complete the landslide mapping, we then found another scene approximately a month after the mainshock and delineated polygons for the landslides that were already partly seen in the earlier images (Figure 5d). Following the same procedure, we mapped all landslides triggered by the mainshock.

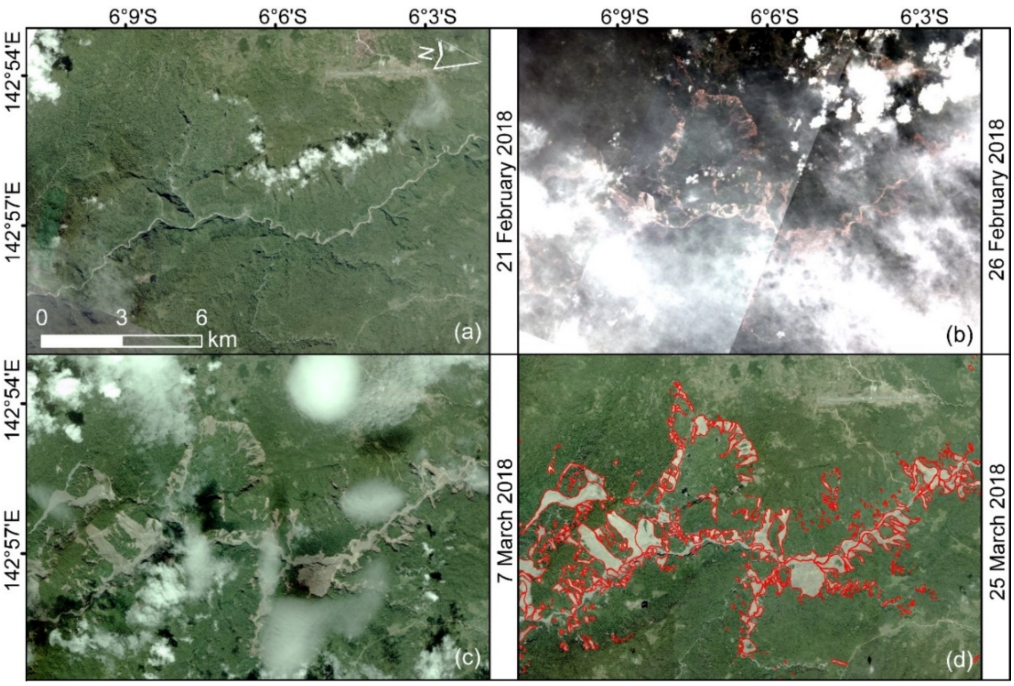

Figure 5. An example showing the usage of (a) pre-seismic and (b, c, and d) multiple post-seismic PlanetScope images to map landslides in an area affected by dense cloud cover soon after the mainshock. Red polygons presented in panel (d) indicate the landslide polygons we mapped. The location of this area is indicated in Figure 6.

2.2 Characteristics of the landslide event

We examined the mapped landslide size statistics in a comparative manner by considering some of the largest EQIL-inventories available through USGS's EQIL repository (Schmitt et al., 2017). For this step, we calculated the landslide-event-magnitude scale using frequency-area distribution (FAD) of landslides (mLS, Malamud et al., 2004; Tanyaş et al., 2018). We examined the size distribution of co- and post- seismic landslides further, by plotting the FADs of both categories and comparing them with FADs computed for some of the largest EQIL inventories occurred in the last few decades across the globe.

We also analyzed potential factors controlling the spatial distribution of landslide occurrences and their size. In this context, we tried to account for a variety of parameters reflecting the complex settings of the study area. Specifically, we considered morphometric (i.e., slope and local relief), seismic (i.e., PGA), climatic (i.e., antecedent rainfall) and geological characteristics (i.e., geologic units and structural features gathered from 1:250,000 geological maps of PNG, Davies and Norvick, 1974; Brown and Robinson, 1982; Davies, 1983). To assess their relevance in controlling landslide occurrence and size, we implemented two analytical schemes: a simpler descriptive summary of landslide characteristics extracted at locations where landslides occurred; and a more complex multivariate regression framework using a Slope Unit (SU) partition, which is geomorphological and hydrological terrain subdivisions bounded by drainage and divide lines (Alvioli et al., 2016).

For the regression analyses, we implemented a Bayesian version of a Generalized Additive Mixed Model (GAMM, Steger et al., 2021), where a binomial likelihood is used to distinguish stable and unstable SUs, whereas a GAMM with a Gaussian likelihood is then used to model landslide planimetric extents expressed in logarithmic scale (see Lombardo et al., 2021). To evaluate the modelling performance, we use receiver operating characteristic curves (ROC) and their integrated area under the curve (AUC, Hosmer and Lemeshow, 2000). We remind the reader that our aim at this stage is not to build an operational landslide predictive model of occurrences and sizes but rather to explore and understand the effects of environmental parameters with respect to co-seismic and post-seismic landslides' characteristics. We emphasize that adopting an SU partition requires an aggregation step whenever environmental parameters are expressed with a higher resolution compared to the coarser SUs. For instance, we chose to summarize the distribution of slope steepness and PGA values per SU by using their mean and standard deviation.

3 Results

3.1 Co- and post- seismic landslide inventories

Overall, we mapped 11,541 landslides with a total area of 185 km^2 (Figure 6). Based on our mapping and imagery interpretation, debris flows, debris slides and mudslides are the most common landslide types. Large landslides are widespread in the study area and more than half of the mapped landslides have a planimetric area larger than 50,000 m^2. Our analyses also show that 10,403 landslides with a total area of 145 km^2 were triggered by the mainshock, whereas the remainder (1,138 landslides with a total area of 40 km^2) were induced by either aftershocks or succeeding rainfall events between February, 26 and March, 19. In this paper, we will refer to the former category as co-seismic and the latter one as post-seismic landslides (Figure 6).

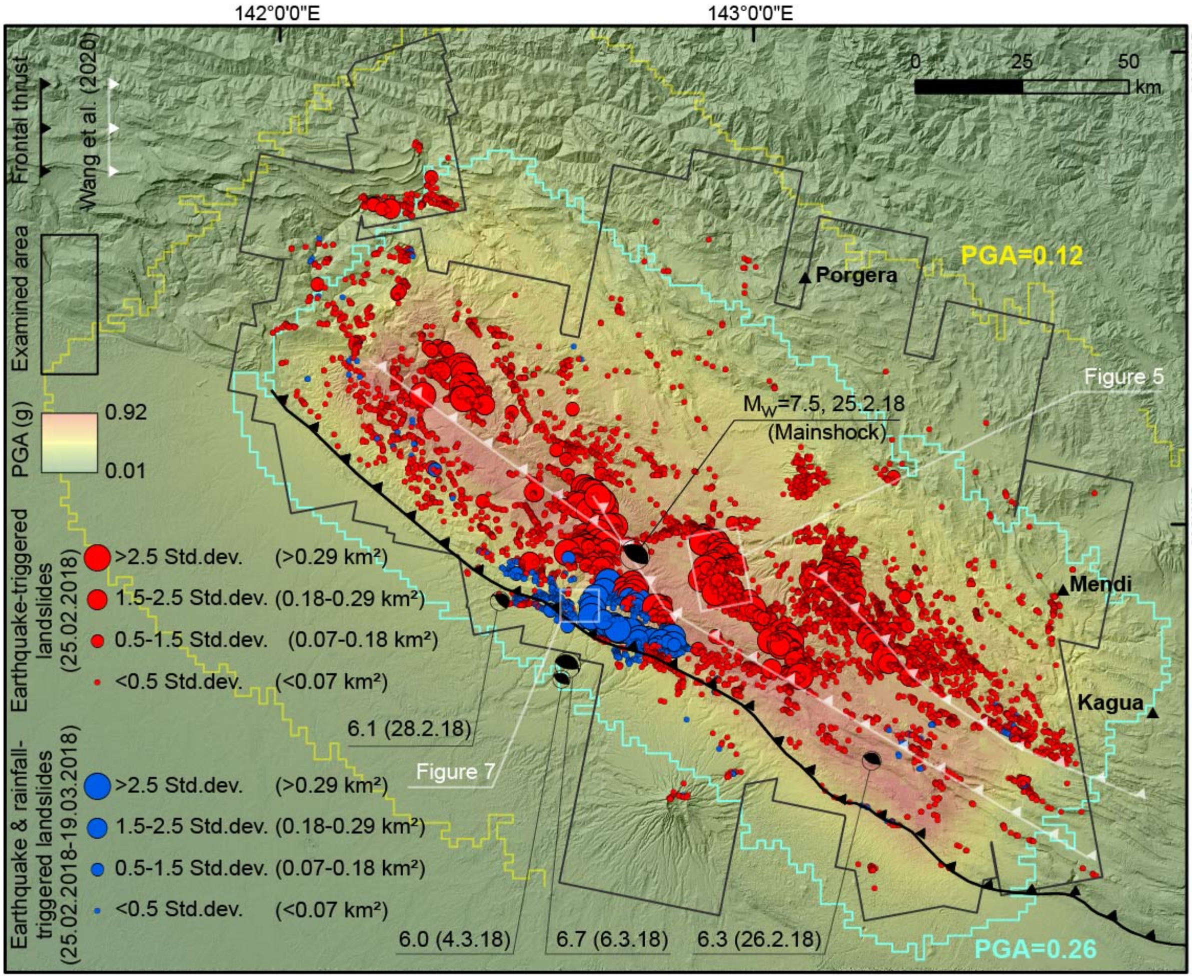

Figure 6. Spatial and size distribution of landslides triggered by the PNG mainshock (red) and its aftershocks or by succeeding rainfall events occurring until March, 19 (blue). The overlain PGA map refers to the mainshock.

We also stress here that some of the landslides we labeled as co-seismic may have been triggered or expanded by the aftershocks or succeeding rainfall events. This is because the area was not only hit by four strong aftershocks from February 26 onwards but also exposed to precipitation. In fact, we differentiated the landslides triggered by the mainshock and the ones induced by the aftershocks or succeeding rainfall events as much as possible based on the availability of cloud free satellite images.

To exemplify our mapping procedure for the reader, we focused on an area that was not only affected by some of the aftershocks (i.e., February 28, M_w=6.1; March 4, M_w=6.0 and March 6, M_w=6.7 earthquakes) but also some strong rainfall events after the mainshock (Figure 6 and 7a). Figure 7 shows that except for a few small landslides triggered in the northeastern part of the subset, the area does not include a large population of landslides based on the comparison between pre-seismic (Figure 7b) and post-seismic images acquired two days after the mainshock (Figure 7c). However, another image acquired on March 19, highlights many landslides and in particular, one large debris flow in the central area of the image (Figure 7e). The footprint of the debris flow is also partly visible in an earlier image acquired on March 7, although we can only see a limited part of the area because of the cloud cover (the blue rectangle in Figure 7d). These observations show that the landslides were most likely triggered between February 27 and March 7. This is the narrowest time window we can identify to be associated with these landslides. However, we do not see the entire area until March 19. Based on these observations, either aftershocks or daily rainfall or any accumulated precipitation amounts could be considered as a possible triggering factor for these landslides. It is notable that there were extreme rainfall events on February 27, with 35 mm of rain and on March 12, with 60mm of rain.

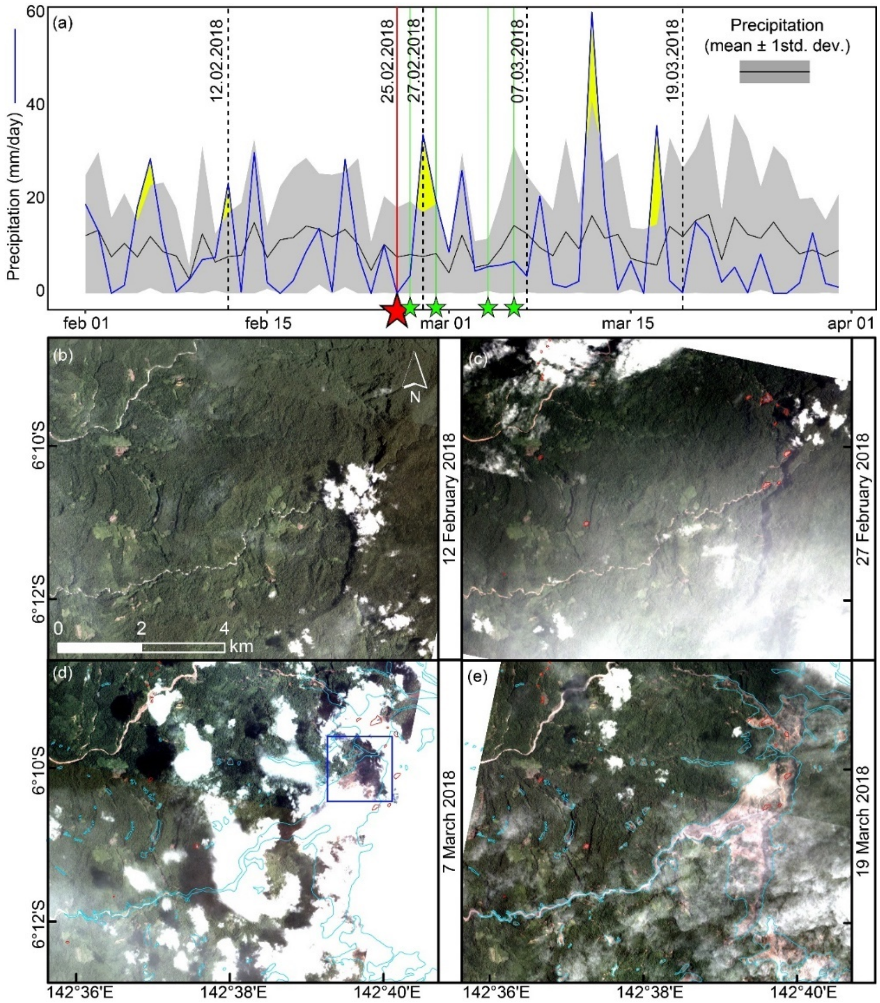

Figure 7. An example site showing landslides triggered by not the mainshock but either aftershocks or succeeding rainfall events. In panel (a) the variation in daily precipitation amount is expressed as the mean and ±1 standard deviation of daily precipitation, calculated from a 20-year time series. The mean value is represented by the solid black line whereas the standard deviation interval is shown as the grey shaded area. The yellow areas highlight extreme rainfall events, where the daily precipitation exceeded the typical 20 years rainfall variability for that specific period (IMERG Final Run product, Huffman et al., 2019). The red star and the solid red line indicate the date of the mainshock, whereas the green stars and the solid green lines represent the aftershocks. The black dashed lines correspond to acquisition dates of images presented in the following panels. Panels (b) shows the pre-seismic conditions, whereas panels (c, d and e) depict the post-seismic situation via multi-temporal PlanetScope images. In panels (c, d and e) red polygons indicate co-seismic landslides and cyan polygons represent post-seismic landslides. The blue rectangle in panel (d) corresponds to the footprint of the debris flow which was clearly mapped (e) as further discussed in the text. The location of this area is indicated in Figure 6.

3.2 Magnitude of the 2018 PNG landslide event

The total landslide area obtained from the co-seismic inventory for this region in PNG was compared to 5 major earthquakes and associated landslide inventories: the 1999 M_w=7.7 Chi-Chi (Liao and Lee, 2000), 2002 M_w=7.9 Denali (Gorum et al., 2014), 2008 M_w=7.9 Wenchuan (Xu et al., 2014), 2010 M_w=7.0 Haiti (Harp et al., 2016), and 2015 M_w=7.8 Gorkha (Roback et al., 2018) earthquakes. Figure 8 reports these five cases sorted by landslide-event-magnitude (Tanyaş et al., 2018), where the Wenchuan case appears to be the first (with a mL=6.2), followed by Chi-Chi (mL=5.1), Denali (mL=4.9), Gorkha (mL=4.6) and Haiti (mL=4.3). In this context, the landslides associated with the PNG earthquake produce a mL of 5.2, thus placing this event right after the extreme case of Wenchuan.

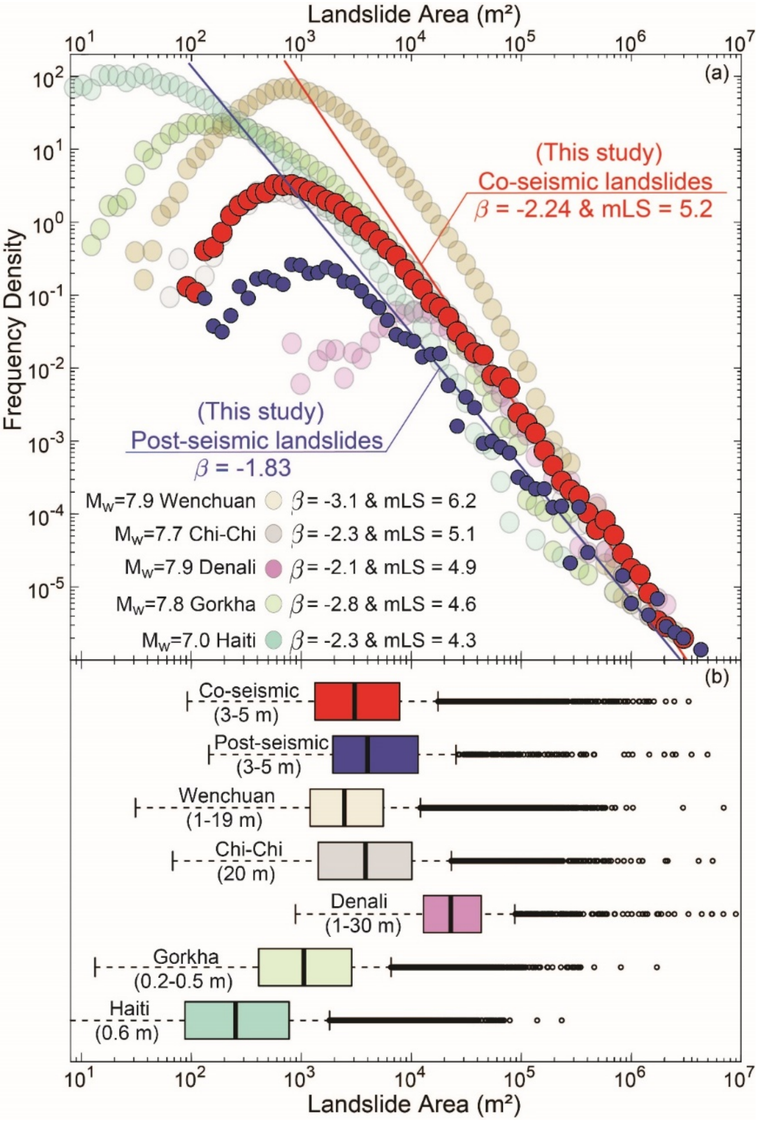

Figure 8. Summary of landslide size characteristics associated with co- and post- PNG induced landslides (red and blue respectively), together with global examples of co-seismic inventories. Panel (a) shows the frequency area distributions for each of the considered inventories, whereas panel (b) presents the box plots summarizing the distribution of the landslide area. In panel (b), values given in parentheses indicate the spatial resolution of images used for landslide mapping. The average power-law exponent of known co-seismic inventories is -2.5 (see Tanyaş et al., 2018).

We also computed the power-law exponents, including the landslides that occurred after the 2018 PNG earthquake. The co-seismic landslide inventory returned a power-law exponent (β=-2.24) in range with the other available co-seismic landslide inventories in the literature (Figure 8a). However, the same metric computed for post-seismic landslides (β=-1.83) produced an exponent which is smaller than most of the other co-seismic inventories available in the literature. This characteristic illustrates the dramatic difference between the frequency of large and small post-seismic landslides (see Figure 8a) and specifically to the abundance of large post-seismic landslides. This can be further checked in Figure 8b, where the distribution of landslide sizes is reported for all the inventories under scrutiny. There, the median landslide area ranks the Denali co-seismic inventory first, followed by the PNG post-seismic inventory, then Chi-Chi, the PNG co-seismic inventory, Wenchuan, Gorkha and Haiti. It is worth noting that a minor biasing effect for this could be the resolution of the satellite scenes used to map the landslide inventories. For instance, the coarse resolution of the scenes used to map the Denali and Chi-Chi inventories may induce amalgamation issues, influencing the associated landslide size distribution. Nevertheless, the median landslide size of both co-seismic and post-seismic landslides that occurred in PNG is still much larger than the median landslide size associated with some strong earthquakes such as Denali and Haiti.

3.3 Factors influencing the initiation of landslides

3.3.1 Geology and structural features

The relationship between geological units mapped throughout the study area and the 2018 PNG earthquake landslide inventory is shown in Figures 9 and 10. Our analysis indicates that the majority of landslides occurred within:

- limestones (Darai Limestone)
- volcaniclastics intercalated with conglomerate and sandstone (Kerewa volcanics) and
- agglomerate, tuff, and lava layers (Sisa volcanics).

The largest landslides were mainly triggered in limestone layers (Darai limestone), weathered agglomerate, tuff, and lava layers (Sisa and Kerewa volcanics) and lacustrine deposits (Kagua clays; Figure 10).

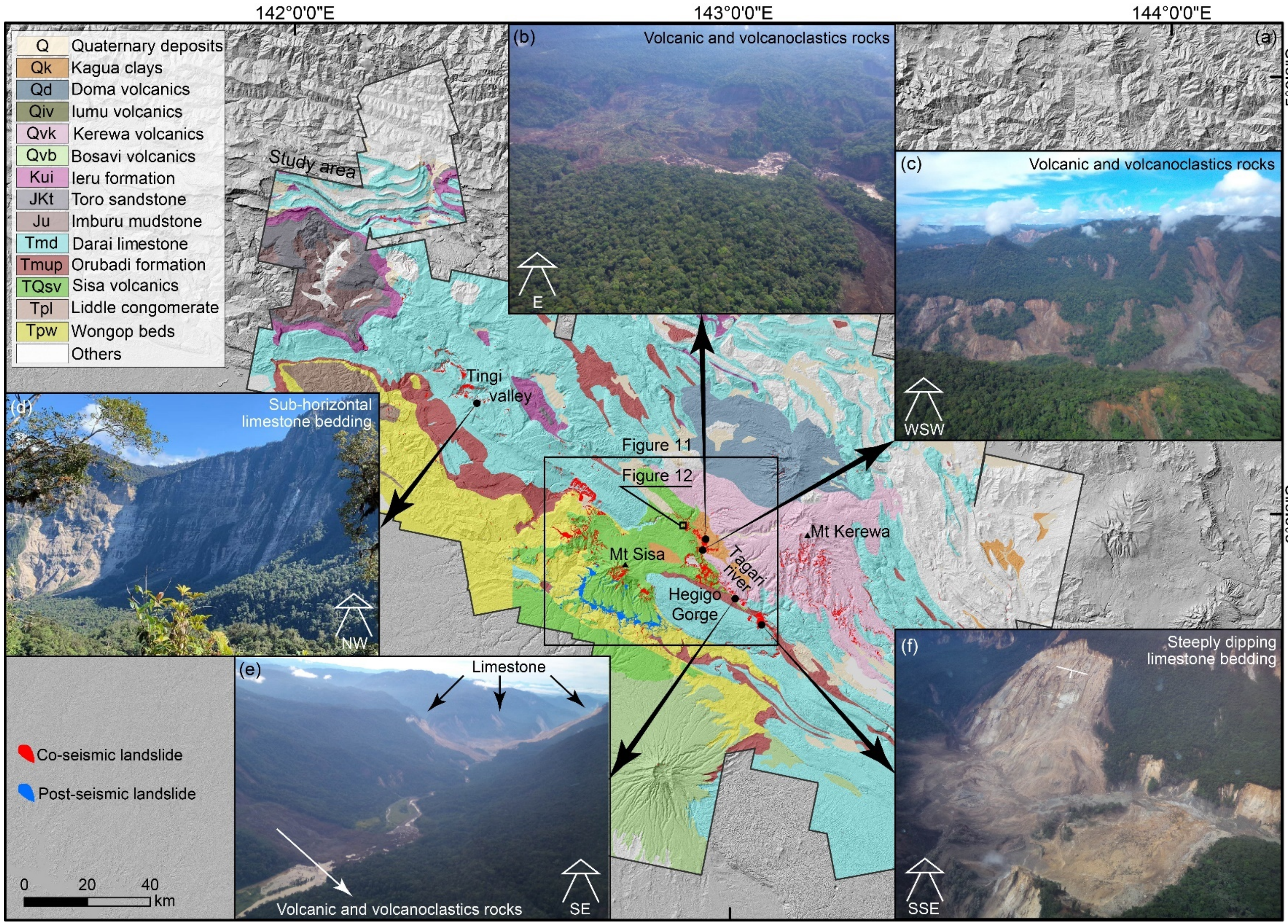

Figure 9. Plot showing (a) the main geological units, spatial distribution of landslides (red polygons indicate co-seismic landslides and blue ones represent post-seismic landslides) and (b-f) examples of the landslides along the Tingi and Tagari Valley affected areas. Photos courtesy of Papuan Oil Search.

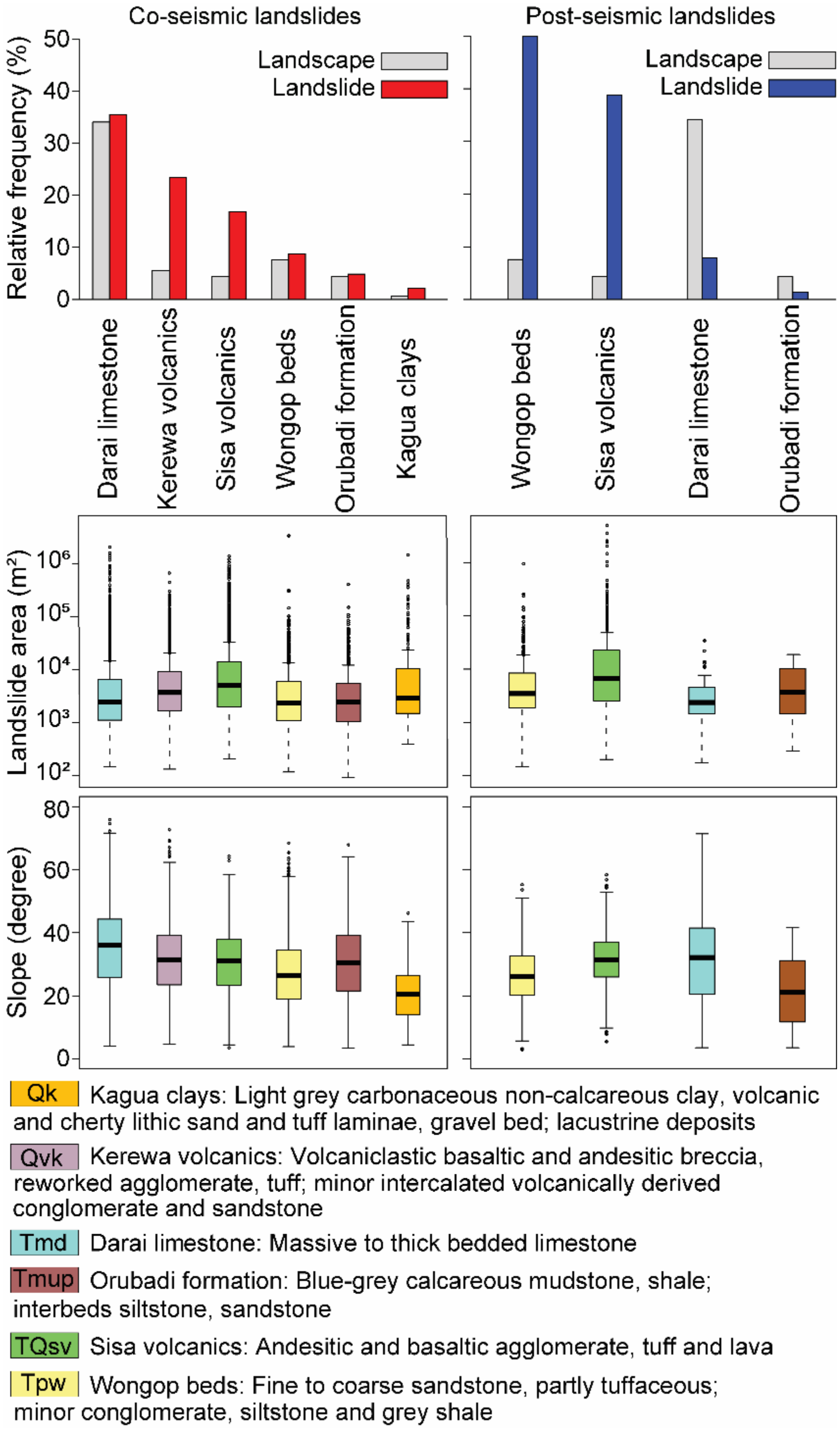

Figure 10. Landslide frequency, size and characteristic slope distributions for the main geological formations in which co- and post- seismic landslides were triggered. The percentages indicate the landslide populations of the presented units over the total co- and post- seismic landslide populations as well as the percentage of the areal coverage of the geological units over the entire study area. If the percentage of landslide population associated to a geological unit is less than 1%, the corresponding unit was not presented in the plot.

Approximately 35% of the whole landslide population occurred within the Darai Limestone, including some of the largest landslides we mapped (e.g., Figure 9 and Figure 10). As previously reported by Mahoney et al. (2021), many of the most catastrophic landslides occurred in the Hegigio Gorge where bedding-parallel weaknesses (e.g., lithological variations) within the thick, strong crystalline limestone formed planes of mechanical weaknesses along which huge masses of rock failed (e.g., Figure 9f). In the Hegigio Gorge, Darai Limestone beds dip out of the slope faces with steep dip angles, at some locations reaching up to 55° (Brown and Robinson, 1982). Based on our mapping and the available geological information, it appears that the occurrence of the largest landslides within the Darai Limestone occurred on steep slopes where the limestone was deformed in such a way that the bedding-parallel planes of weaknesses were also steeply dipping (e.g., sub-parallel to the steep slope; Figure 9f). In comparison, where the limestones were relatively undeformed and the bedding-parallel weakness planes were flat-lying, the area and volume of displaced rock were much less significant, even in areas characterized by steep slopes (e.g., c.f., Tingi Valley and Hegigio Gorge photos in Figure 9d). Both the number and the average size of landslides are relatively smaller in the western part of the study area where the bedding angle is low (sub-horizontal) compared to the eastern part (Figure 9a).

The Kerewa and Sisa volcanics only cover ~10% of the landscape in the area under consideration. However, these units together had most of the landslides (i.e., 40% of the whole landslide population including both co- and post- seismic ones). The spatial distribution of landslides plotted over the geological map shows that they almost exclusively occurred in the calderas and on the flanks of the Pliocene to Pleistocene Mount Kerewa and Mount Sisa volcanoes (Figure 9a). Collectively, more landslides occurred within Kerewa and Sisa volcanics than in the Darai Limestone, despite the much smaller areal coverage of the former across the study area (e.g., Figures 9 and 10). Our interpretation is that the generally weaker lithologies and interbedded nature of the volcanic and volcaniclastic rocks make them particularly predisposed to failure (e.g., Figures 9b and 9c), especially within the steep slopes around radial drainage channels (e.g., Mt Kerewa; Figure 9a) and around sub-linear structural features such as fault scarps and folds (e.g., SW flank of Mt Sisa; Figure 9a).

To take a closer look at these structural features at an exploratory level, we examined a subset of the landslide-affected area where landslides concentrate along discontinuity surfaces (Figure 11). For instance, in the southern part of the examined subset, a series of landslides are well aligned with the contact between andesitic/basaltic agglomerate, tuff and lava layers (Sisa volcanic, TQsv), and sandstone layers (Wongop beds, Tpw). Similarly, landslides located along thrust faults on the flanks of Mount Sisa volcanics. Also, some landslides which were initiated along a hinge of an anticline appear in limestone layers (Darai limestone, Tmd) in the northwestern part of the area. The spatial distribution of these landslides implies that they were likely triggered along bedding planes.

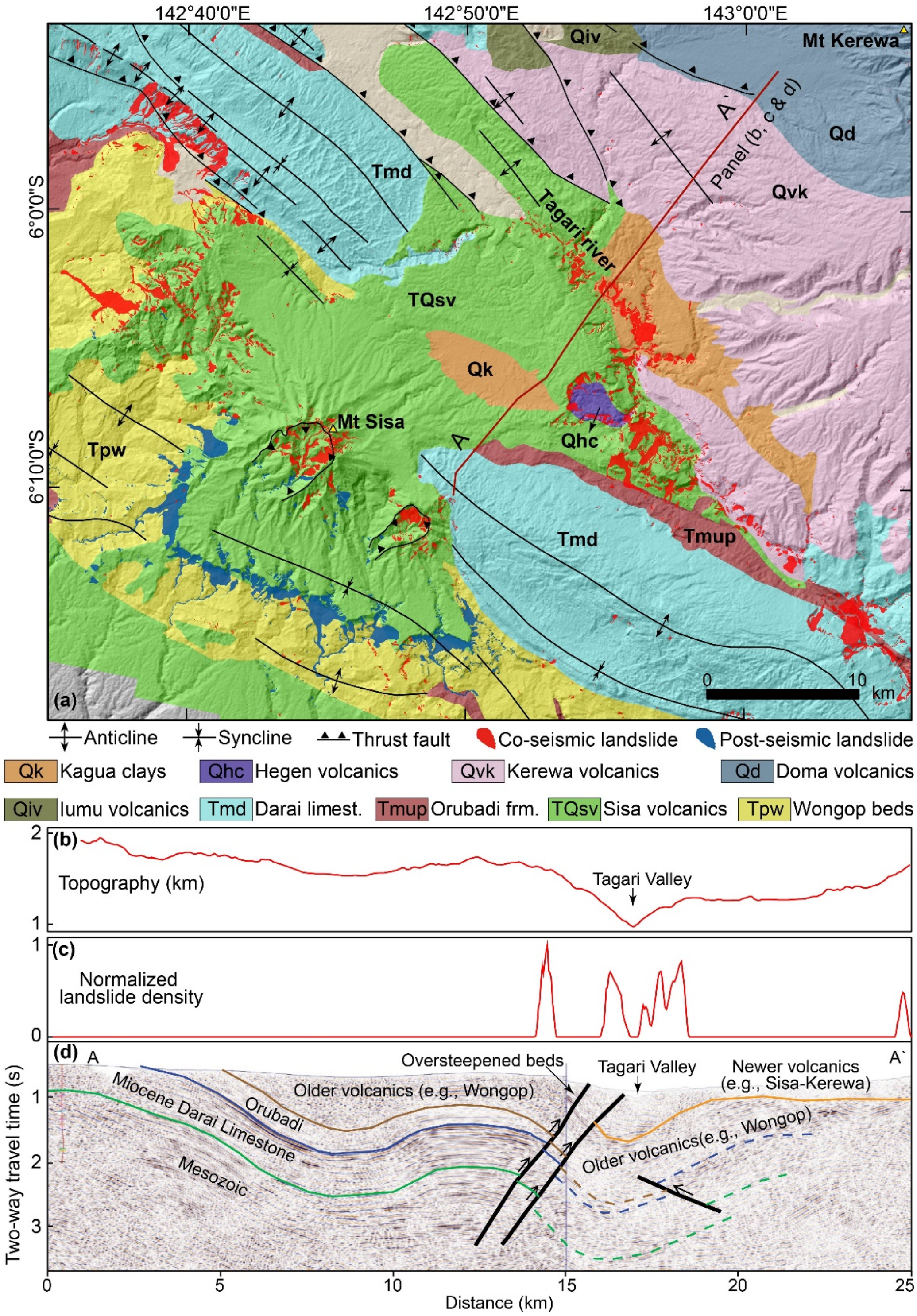

Figure 11. Plot showing (a) the geological units and structural features of a subset of the landslide affected area where A-A' shows the location of the profiles and seismic sections in (b-d). Panel (b) shows the topography, whereas panel (c) represents the normalized landslides density attributes' profiles along the seismic section A-A' in panel (d). The reflection seismic section across the Tagari Valley showing the folded and thrust faulted Darai Limestone, Orubadi and Wongop beds (older volcanics). These are unconformably overlain by the very young Newer Volcanics, comprising mainly the stratacones of the Mount Kerewa, Mount Sisa and other volcanoes. The beds adjacent to the Tagari River are interpreted to have been oversteepened by recent thrusting.

We also examined the connection between structural features identified along a seismic section and the spatial distribution of landslides expressed in terms of landslide density (Figure

11). Figure 11d shows that landslides concentrate around the Tagari valley where oversteepened beds intensify slope instabilities. It is worth stressing that the oversteepened beds may not be the major issue alone but the faulted fold as well as the boundary between different units subjected to multi-level stress during the faulting and folding and due to the spatial differential stress pattern associated with the difference in material strengths could make these hillslopes more susceptible. In other words, oversteepened beds are not only a sign of structural complexity but also the associated tectonic deformations on hillslope materials. Notably, these features also reflect the fatigue damage caused by the active tectonics, which likely plays a role in the occurrence of landslides.

The detailed examination conducted on Google Earth images also revealed that hillslope materials were disturbed and became more susceptible following the seismic swarm. For instance, Figure 12 shows some landslides initiated in Kerewa volcanics (i.e., volcaniclastics intercalated with conglomerate and sandstone) that created some tension cracks.

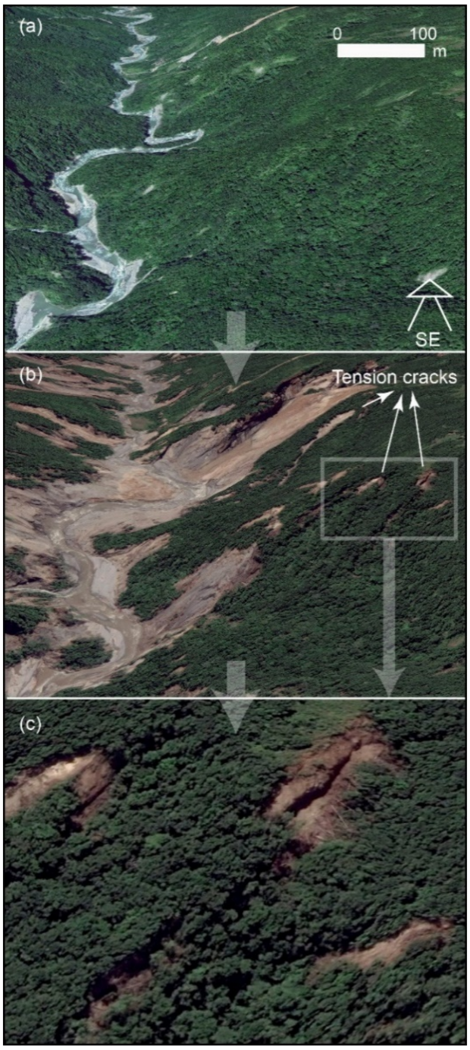

Figure 12. Google Earth images showing the examples of the landslides along the Tagari Valley affected area. Panels show pre- (a) and post- (b and c) images of an area where failures created some tension cracks. Location map is shown in Figure 9.

3.3.2 Precipitation

Tension cracks increase landslide susceptibility because they can cause an increase in rapid pore pressure due to the filling of cracks in case of rainfall events (e.g., Leroueil, 2001). Therefore, we analyzed daily (Figure 13) and antecedent (Figure 14) precipitation amounts in the study area. For daily precipitation, we examined a 20-day time window including 10 days before and after the mainshock. Figure 13 shows that the southern part of the area affected by landslides was partially exposed to strong rainfall events (e.g., on February 21 and 24, ~80 mm/day) in the 10 days before the mainshock. We recall that monthly average precipitation amounts calculated for February and March for the southern part of the study area (e.g., Mount Bosavi) are ~280 mm and ~400 mm, respectively (see Figure 3). Therefore, ~80 mm/day is above the average daily precipitation. Within 10 days following the mainshock the areas were subjected to less intense rainfall events (i.e., <80 mm/day). We calculated antecedent precipitation for 7, 15 and 30 days (Figure 14). Results do not show any direct correlations between the spatial distribution of antecedent precipitation patterns and co-seismic landslides. Also, landslide frequencies show that the majority of landslides are not associated with high precipitation in terms of 7, 15 or 30 days of cumulative amounts (Figure 14).

Antecedent precipitation may still have played a role as a predisposing factor for co-seismic landslides. To explore this possibility, we examined other EQIL inventories for which the literature reported the potential influence of antecedent precipitations (e.g., Mid-Nigata, Sassa et al., 2007 and Hokkaido, Wang et al., 2019). We provide an overview of rainfall conditions prior to the earthquake occurrence for each of the considered cases. Specifically, the rainfall discharged in each site (i.e., landslide affected area) where the corresponding earthquake occurred is shown cumulatively, within a 15 days window. There, the 2018 PNG inventory stands out as the one with the largest exposure to rainfall, followed by the Mid-Nigata, for which Sassa et al. (2007) already stressed its pre-conditioning role in co-seismic landslide occurrence. However, an improved understanding of the contribution of antecedent precipitation in the PNG case required further examination reported in the multivariate analyses below.

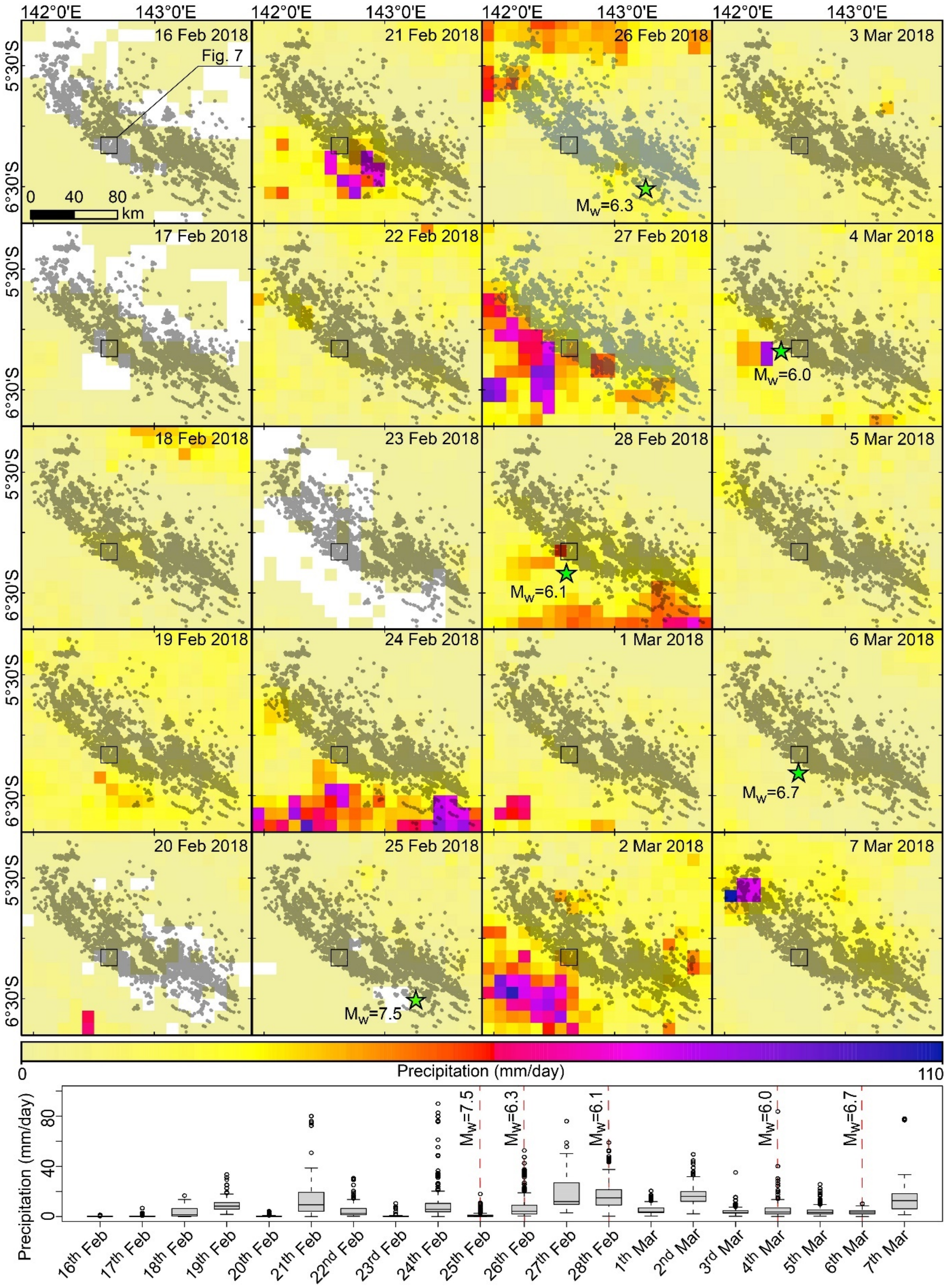

Figure 13. Daily precipitation amounts of the whole study area for a time window covering 10 days before and after the mainshock presented in map format (top panel) and as boxplots (bottom panel). Precipitation amounts are based on IMERG Final Run product (Huffman et al., 2019). Green stars indicate the epicenter of main and aftershocks. The spatial distribution of landslides is shown as grey-shaded points. The black square shows the area presented in Figure 7.

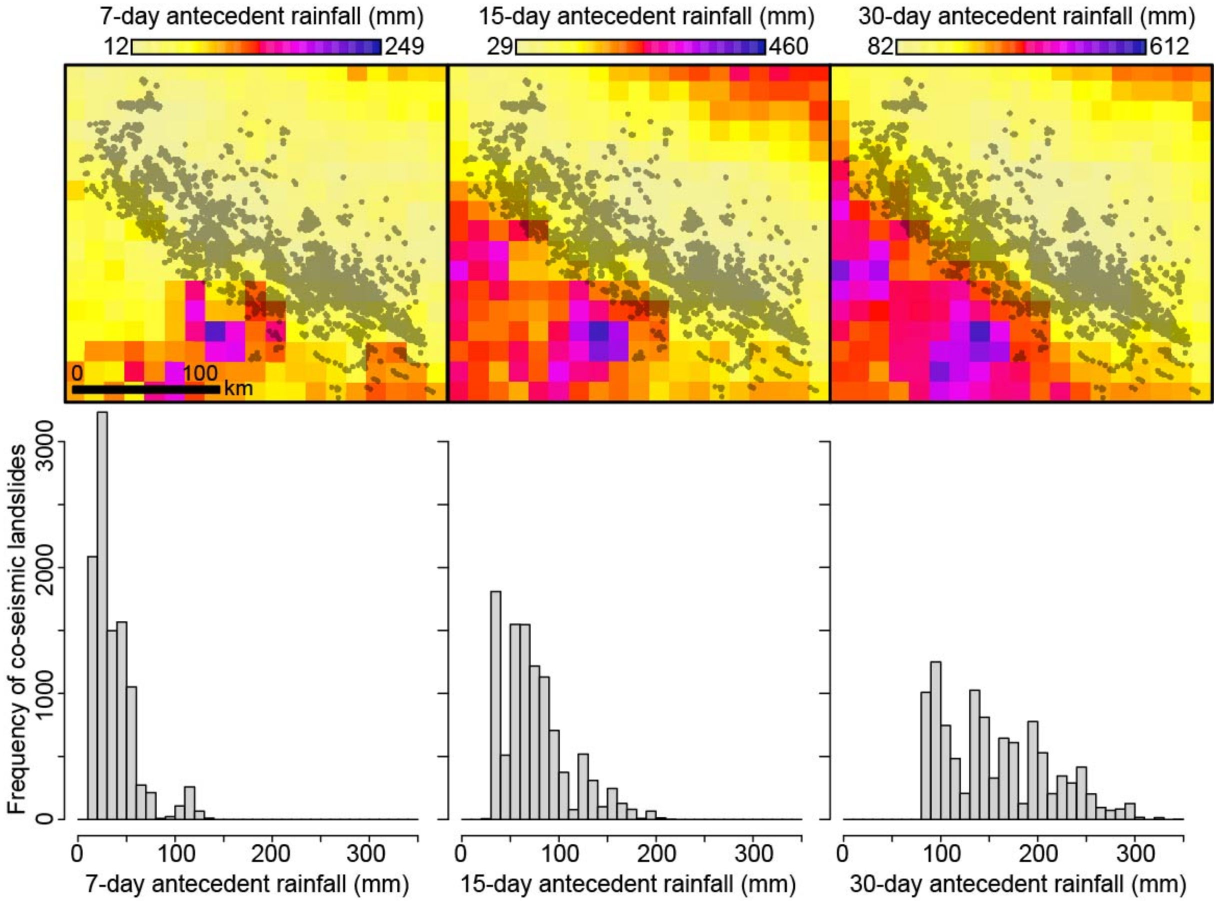

Figure 14. Precipitation amounts calculated for 7, 15 and 30 days accumulated rainfall expressed as maps (top panel) and landslide frequencies (bottom panel). Precipitation amounts are based on IMERG Final Run product (Huffman et al., 2019).

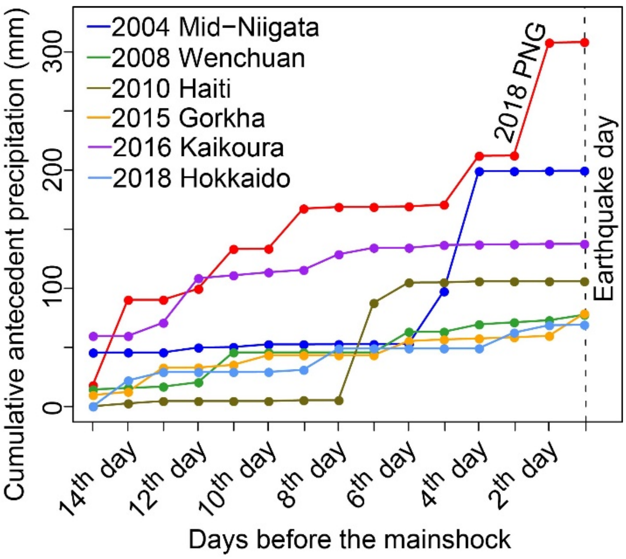

Figure 15. Potential effect of rainfall conditions on the landslide size distribution for each of the considered earthquakes. This is shown as the maximum accumulated precipitation, 15 days before the earthquake occurrence date. Precipitation amounts are based on IMERG Final Run product (Huffman et al., 2019).

3.3.3 Ground shaking and slope steepness

We also examined the spatial distribution of co-seismic landslides in relation to fault rupture zones from the four-fault planes finite-fault model of Wang et al. (2020) (see white thrust faults in Figure 6). Figure 16 shows that the cumulative landslide population logarithmically increases away from the fault rupture zone, as observed in the literature where it is related to the intensity of seismic shaking decreasing away from the rupture (e.g., Keefer, 2000; Massey et al., 2018). Half of the landslide population is concentrated within a 7 km wide buffer zone around the fault planes whereas a 20 km wide buffer zone encompasses approximately 90% of the landslide population.

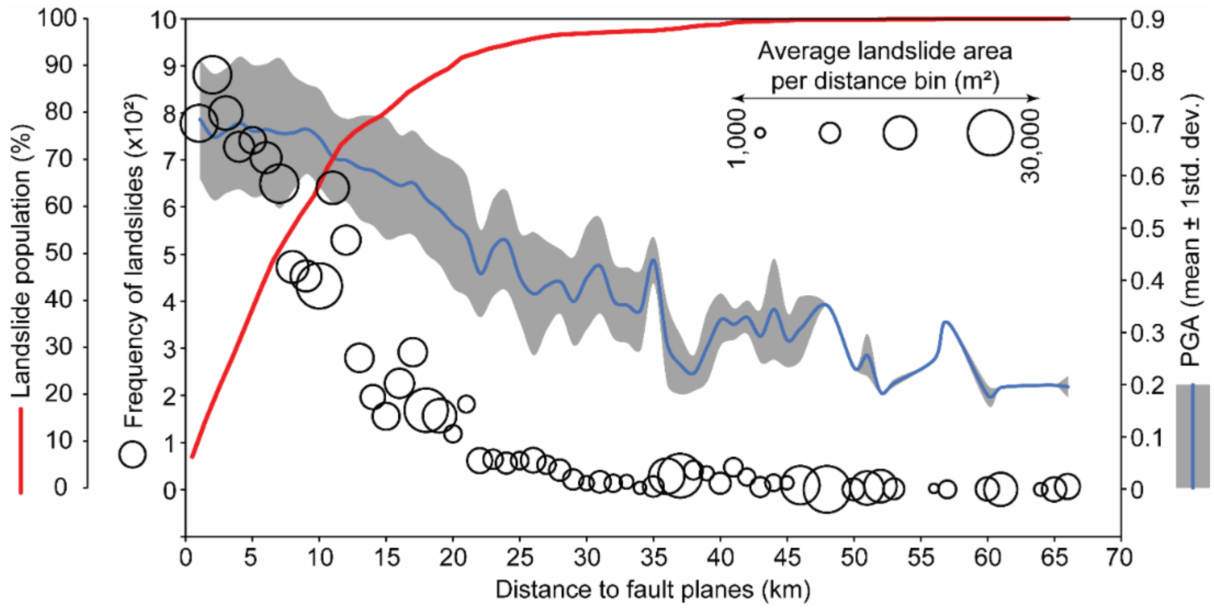

Figure 16. Spatial and size distribution of co-seismic landslides with respect to proximity to fault rupture and PGA values. The solid red line represents the cumulative frequency of the landslide population. The solid blue line represents the mean PGA computed for each distance-to-rupture bin, whereas the grey area consists of the variability per bin, computed as one standard deviation. Black circles express the actual frequency of landslides per distance-to-rupture bin.

We also examined the variation in the frequencies and sizes of both co- and post- seismic landslides with respect to slope steepness. Figure 17 shows that majority of landslides occurred on steeper hillslopes. Only ~14% of co- and post- seismic landslides occurred on hillslopes less steeper than 20°. Figure 17 also shows that the co-seismic landslides mostly occur on steeper slopes compared to their post-seismic counterparts. The mean slope for the co-seismic landslides is 32°, whereas it is 29° for the post-seismic ones. Large co-seismic landslides (e.g., >20,000 m^2) mainly occurred on steeper hillslopes (e.g., 55°<slope<75°). Conversely, large post-seismic landslides appear on both steep (e.g., 40°<slope<60°) and gentle slopes (e.g., ~10°). Overall, in the post-seismic period, average landslide sizes calculated for each slope bin are relatively larger than the co-seismic phase.

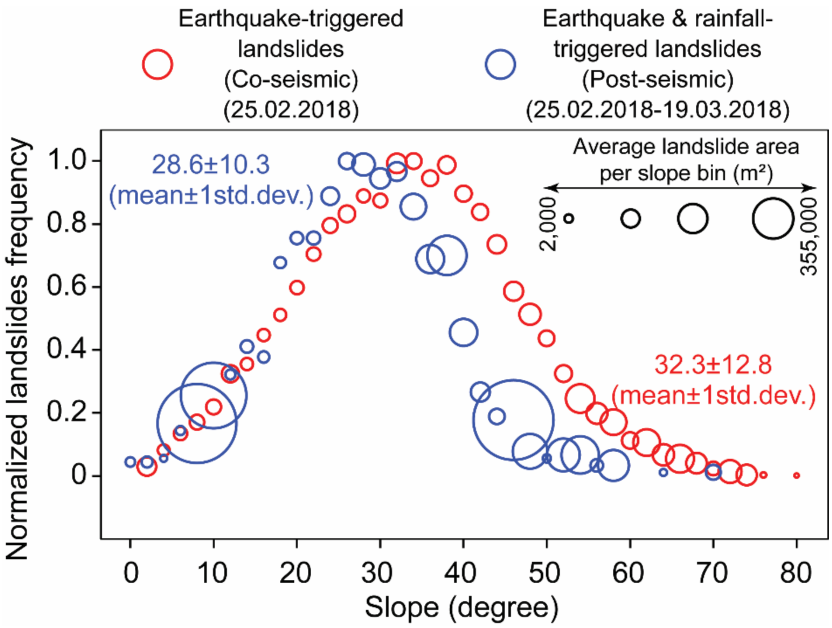

Figure 17. Graph showing the frequency of landslides and average landslide size for various slope bins.

3.3.4 Multivariate analyses

We complemented these simpler bivariate statistics with more complex multivariate models, one for co-seismic landslide location and one for post-seismic landslide size. These have been chosen according to some interesting landslide characteristics we noted between co- and post-seismic failures that we discuss below.

The first model we tested corresponds to a common susceptibility model built to investigate the spatial distribution of co-seismic landslides. For this susceptibility model, we adopted a structure where all covariate effects have been tested in a nonlinear framework, by using a Bayesian version of a more common binomial Generalized Additive Mixed Model (GAMM; e.g., Steger et al., 2016). The results are shown in Figure 18, where panels (a) and (b) briefly present the performance of the classifier. Specifically, the posterior mean probabilities of landslide occurrence per SU suitably distinguish stable and unstable SUs. This is evident in panel (a) where the median of the probability spectrum for stable SU is close to zero, whereas the same median for unstable SU is approximately 0.3 and significantly different from the non-susceptible counterpart. This net classification is reflected in the AUC reported in panel (b), where the 0.92 value corresponds to an outstanding goodness-of-fit performance according to Hosmer and Lemeshow (2000). Having demonstrated the accuracy of this GAMM classifier, we present each model component in panels (c) to (i). These plots report on the y-axis the regression coefficients estimated for each covariate class, these being shown in the x-axis. The interpretation of these coefficients is that negative regression values imply decreased probability of landslide occurrence. Positive values imply increased probability of landslide occurrence and values centered around zero do not contribute to the probability estimates.

The trend of the relation between the regression coefficients and the covariate classes can vary from simple linear (e.g., Figure 18h) to complex nonlinear relation (e.g., Figure 18c). The results of the analysis will be reported below.

The multivariate analysis of the co-seismic landslides' locations and seven model parameters namely; 15-day antecedent precipitation before the mainshock, hillslope steepness average and its standard deviation, slope unit area, average PGA per slope unit and its standard deviation are shown in Figure 18c to 18i; respectively.

The rainfall aggregated within a 15-day time-window before the mainshock is shown to behave nonlinearly with a near-sigmoidal shape that starts with a negative regression coefficient that shifts to a positive one at around 180 mm (Figure 18c). Thus, from a marginal perspective, i.e., assuming all the other parameters fixed, the landslide susceptibility is high when 15-day aggregate rainfall is >180mm.

The signal of the slope steepness appears to be almost linear. This is contextually shown for the mean (Figure 18d) and standard deviation (Figure 18e) of the slope steepness per SU, where mean values above ~27° and their variability above ~10° are associated with likely unstable SUs. Therefore, fixing all the other model parameters, the landslide susceptibility is high when mean slope dip is >27 deg with 10 deg variability.

The effect of the local relief appears nonlinear (Figure 18f), with an increase up to ~1000 m followed by a flat to slight decrease to ~1800 m and then a near-exponential growth of the estimated regression coefficient as the relief increases. Thus, from a marginal perspective, i.e., assuming all the other parameters fixed, the landslide susceptibility increases rapidly when relief is >1800m.

The size of the SU also appears to be slightly nonlinear and positively associated with the probability of co-seismic landslide occurrence for SU larger than ~0.02 km^2 (exp[10 m^2]; Figure 18g). In this case, the SU-area threshold marking the shift from negative to positive contributions to the susceptibility is approximately 0.44 km^2 (exp[13 m^2]; Figure 18g). Thus, by solely considering the slope unit size, areas with a slope unit of >0.44 km^2 have a higher risk of landslides.

The signal of the PGA appears to be strongly contributing to landslides occurrence when it comes to the mean acceleration estimated per SU (Figure 18h), and negligible when considering its variability per SU (Figure 18i). This may be because the PGA is quite coarsely estimated (~1 km resolution) in the raw data itself, thus the variability per SU is small to none to begin with. Nevertheless, the mean PGA appears to contribute to the co-seismic landslide susceptibility in a quite linear fashion where the mean regression coefficient smoothly increases as the PGA increases, changing its sign at around 0.5 g. This means that 0.5 g marks a change of the PGA contribution to the estimated probability of landslide occurrence, when considering the co-seismic failures' behavior.

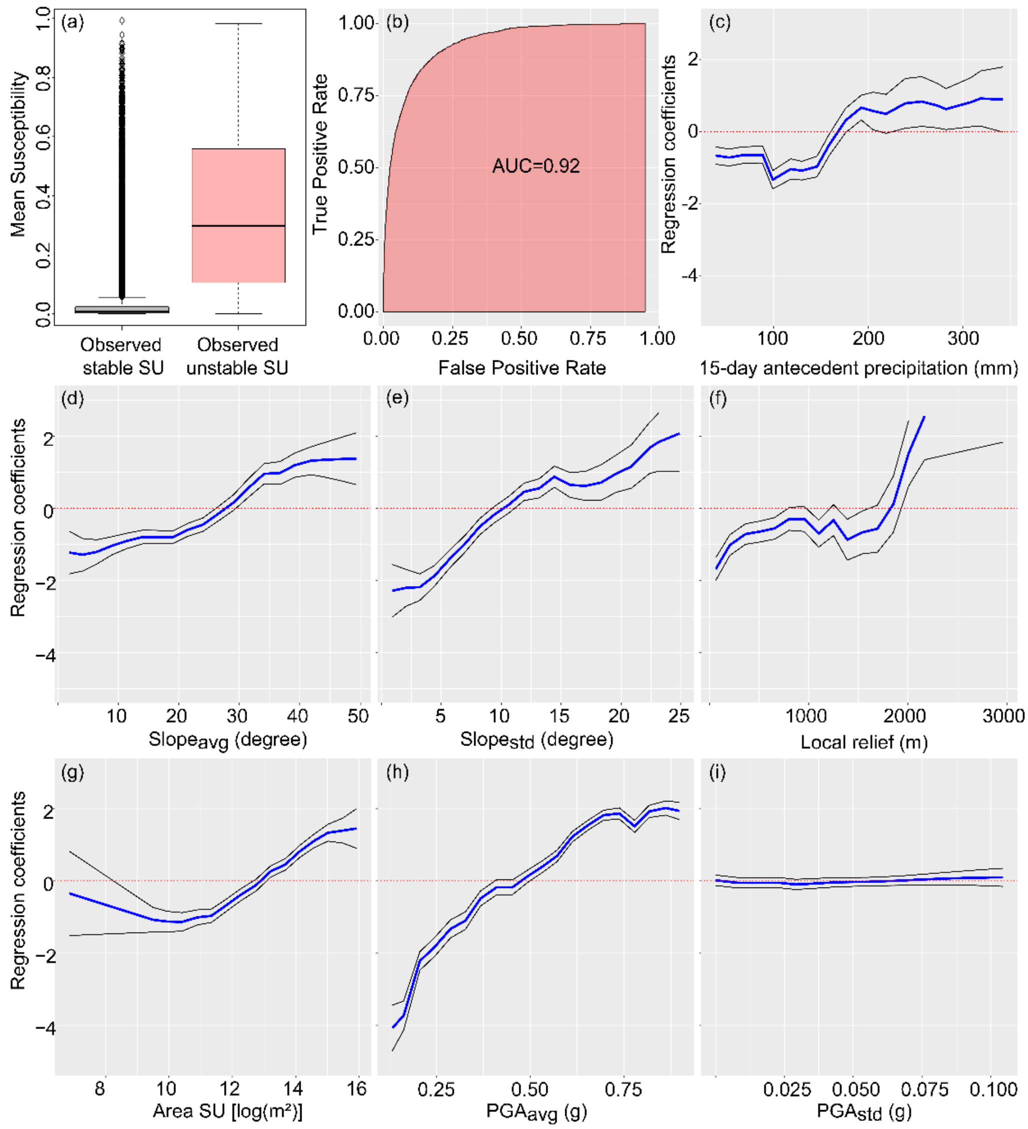

Figure 18. Summary of the binomial GAMM: panel (a) shows the distribution of the posterior mean probability of landslide occurrence, summarized into two boxplots, one for stable and one unstable SUs; panel (b) reports the ROC curve and associated AUC whereas panels (c) to (i) highlight the nonlinear effects estimated for 15-days antecedent rainfall, average slope steepness per SU, standard deviation of slope steepness per SU, Local Relief, SU extent, average PGA per SU, and standard deviation of PGA per SU, respectively. Solid blue lines represent the posterior mean of the regression coefficient, these been bound by the 95%CI (credible interval) represented by solid black lines. The dotted red line corresponds to non-contributing effects.

The multivariate analyses on the estimation of landslide sizes also produced interesting results. We stress here that the landslide size we modeled belonged to post-seismic occurrences. The reason behind this choice is because they showed a peculiar behavior, with very large variations of the planimetric areas and with the largest failures belonging to the post-seismic phase rather than the co-seismic one (see Figure 8 and 17). Moreover, post-seismic landslides are all clustered in a single sector (see blue circles in Figure 6) where several aftershocks swarmed from late February to early March 2018. For this reason, we considered a model for landslide size to be a quite interesting experiment to run and hypothesized that the recurrence of mainshock and aftershocks may be responsible for the unique distribution of landslide planimetric areas highlighted in Figure 17. To test this hypothesis, we first had to come up with a proxy for the accumulated effect of several shakings on slope stability. We addressed this issue by computing the cumulated PGA per SU of the four aftershocks with $M_w \geq 6$. In addition to this "aftershock" covariate and a few traditional morphometric ones, we also considered the PGA of the mainshock as a predisposing factor. We chose to do so, to account for the legacy effect that the PNG earthquake may have exerted onto the landscape (Tanyaş et al., 2021). And, we also used the 15-day antecedent rainfall to the mainshock as a proxy for soil moisture conditions. We opted for this rainfall signal because we did not know the exact date of post-seismic landslide occurrences.

To model post-seismic landslide sizes, we opted for a log-Gaussian GAMM. In other words, the target variable is the planimetric area of post-seismic landslides, expressed in logarithmic scale. This choice is meant to gaussianize the distribution and make it suitable for a statistical model which assumes that the distribution of the transformed landslide sizes behaves according to a Gaussian distribution (Lombardo et al., 2021).

The results shown in Figure 19 indicate that the observed planimetric areas per SU are well in agreement with their estimated counterpart. Specifically, 70% of the observed planimetric area variability is explained by the estimated landslide areas, and the majority of the discrepancies between the two are mostly confined for failures with an observed size less than ~150 m^2 (exp[5 m^2]; Figure 19).

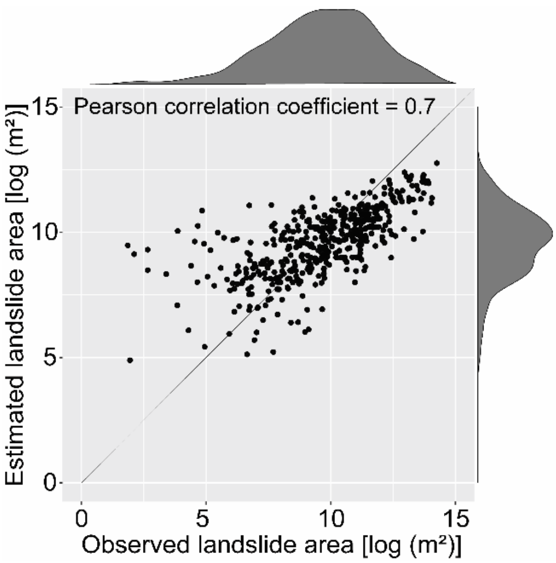

Figure 19. Observed landslide planimetric areas aggregated per SU and expressed in logarithmic scale, plotted against the estimated landslide planimetric areas per SU, also expressed in logarithmic scale.

Analogous to the binomial-GAMM results, having demonstrated the accuracy of the model we implemented, we can focus on the interpretation of the single components, as reported in Figure 20. Similar parameters to the multivariate analysis of the co-seismic landslides' location (Figure 18) were used for the post-seismic landslides' sizes in addition two extra parameters of the computed average and standard deviation of the cumulated PGA per SU of the four aftershocks (Figure 20).

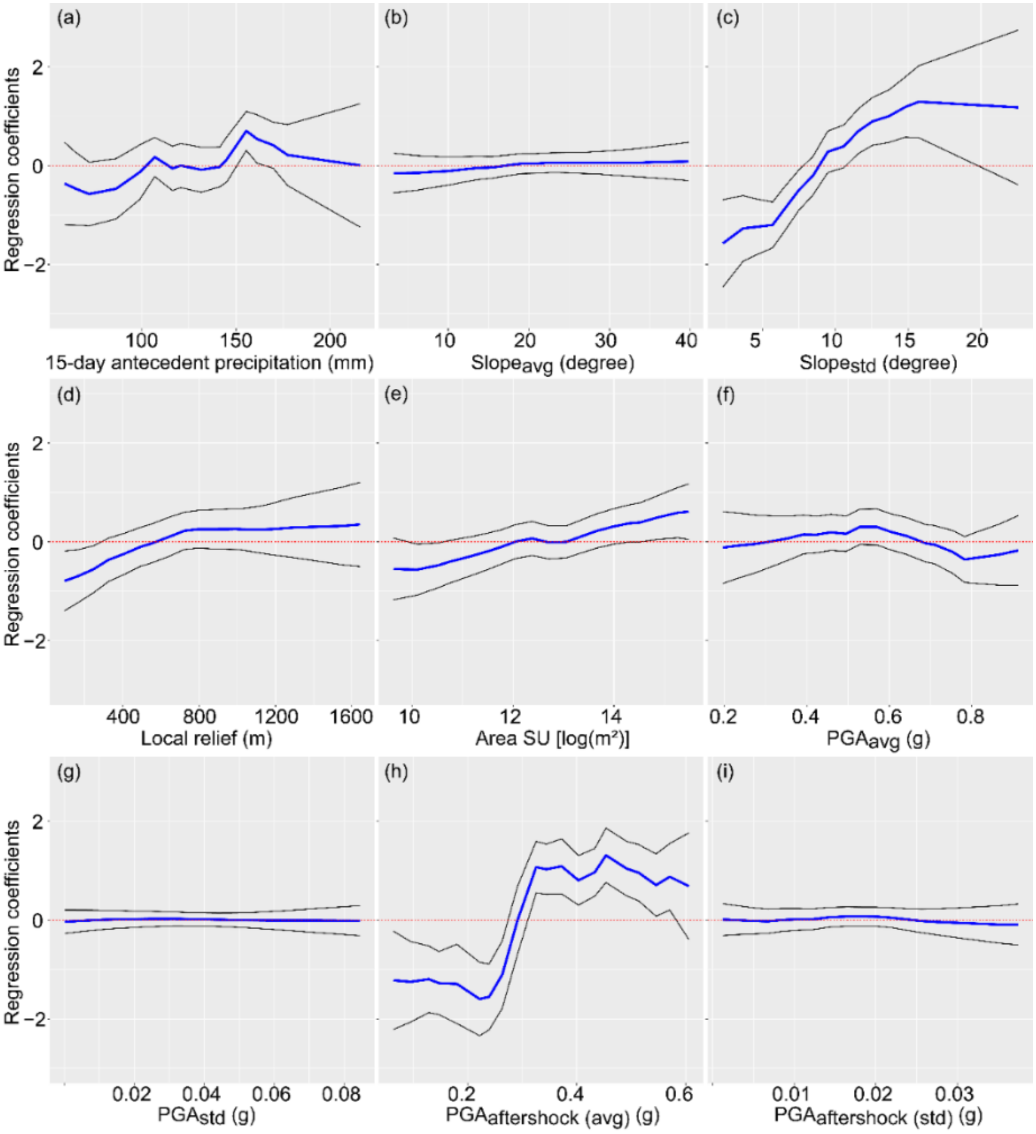

Figure 20. Summary of the log-Gaussian GAMM: Panels (a) to (i) highlight the nonlinear effects estimated for the covariates under consideration. Solid blue lines represent the posterior mean of the regression coefficient, these being bounded by the 95% CI represented by solid black lines. The dotted red line corresponds to non-contributing effects.

The 15-day aggregated rainfall (Figure 20a) appears to be mildly nonlinear and mostly close to being non-significant through the entire range of rainfall values. The average slope steepness seems to be non-significantly contributing to post-seismic landslides size (Figure 20b) while the standard deviation of the slope steepness per SU seems to be nonlinear with no contribution up to 7° followed by linear increasing contribution up to 16° with no significant contribution at larger values (Figure 20c). The relief (Figure 20d) shows a mild nonlinear relation to post-seismic landslide sizes, with its average regression sign shifting to positive at around 600 m in elevation change. Conversely, the SU area appears to be linearly related to post-seismic landslide sizes (Figure 20e).

As for the effect of the ground motion, an interesting situation arose. The average and standard deviation of the mainshock PGA appears to be non-significant, with the zero line (dotted red line in Figures 20f and 20g) being contained within the 95% posterior regression distribution. However, the cumulated PGA computed for the aftershocks is markedly nonlinear, significant and sigmoidal in shape, with an abrupt change in contribution to post-seismic landslide areas at around 0.3 g (Figure 20h) while the standard deviation of the accumulated aftershocks PGA (Figure 20i) appears to be non-significant due to the coarse resolution of the PGA layer as explained before. The observation of the contribution of the cumulated PGA computed for the aftershocks is remarkable since there is no reference in the current scientific literature that reported the combined effect of aftershocks to post-landslide sizes.

4 Discussion

4.1 Quality and completeness of the co-seismic landslide inventory

Manual landslide mapping is a subjective procedure. Therefore, quality and completeness levels of landslide inventories need to be examined to better understand the possible limitations of an inventory. Tanyaş et al. (2017) proposed a set of criteria to better assess the suitability of any given EQIL inventory for different types of applications (Table 1). Following this approach, we made a self-evaluation for our co-seismic landslide inventory. Our evaluation shows that the inventory meets 80% of the essential conditions (see category A in Table 1) and therefore, it is a suitable dataset to make a landslide susceptibility or hazard assessment and to investigate the distribution, types, and patterns of landslides in relation to morphological and geological characteristics (Tanyaş et al., 2017).

In the evaluation, the low scores are caused by two factors. The first factor is associated with post-seismic landslides. Specifically, some of the post-seismic landslides may have not been differentiated from the co-seismic inventory because both the aftershocks and rainfall events started hitting the area right after the mainshock. We should stress again that the first strong aftershock (i.e., Mw≥6) occurred on February 26, hours after the mainshock. We believe that we have differentiated the majority of co-seismic landslides from their post-seismic counterparts. The second factor pertains to the minimum mapped landslide size, where mapping is nearly complete. In the frequency-area distribution of landslides, the rollover point is assumed at the maximum value before the curve inverts its trend (Tanyaş et al., 2019b). Therefore, small rollover values imply a lower level of amalgamation and higher completeness.

The rollover size in our inventory is between 600-900 m^2 (i.e., linear resolution of roll-over point = 25-30 m, Table 1). Therefore, we scored this criterion as 0.4 over 1.

Table 1. Evaluation of the 2018 PNG co-seismic landslide inventory based on the criteria suggested by Tanyaş et al. (2017).

	Criteria	Execution performance	Score		Category (A)	Category (B)
i)	Was the study area analysed systematically by visual interpretation?	0-100%	0-1	1	Essential criteria (80%)	Essential criteria (70%)
ii)	Was the boundary of the mapped area indicated?	No/Yes	0/1	1	Essential criteria (80%)	Essential criteria (70%)
iii)	Were the pre- and post-earthquake landslides eliminated from the inventory?	0-100%	0-1	0.8	Essential criteria (80%)	Essential criteria (70%)
iv)	Was the mapping resolution of inventory enough to differentiate the individual landslides? (L=Linear resolution of roll-over point)	L>25m : <0.5 25m≥L>5m : ≥0.5 5m≥L : 1	0/1	0.4	Essential criteria (80%)	Essential criteria (70%)
v)	Were the landslides mapped as polygons?	No/Yes	0/1	1	Preferred criteria	Essential criteria (70%)
vi)	Did landslide polygons differentiate source and depositional areas?	No/Yes	0/1	0	Preferred criteria	Essential criteria (70%)
vii)	Were the landslides field checked in problematic areas?	0-100%	0-1	0	Preferred criteria	Preferred criteria
viii)	Were the landslides classified according to type?	No/Yes	0/1	0	Preferred criteria	Preferred criteria

Our co-seismic landslide inventory also meets 70% of the criteria (Table 1) indicated to be essential to study the evolution of landscapes dominated by mass-wasting processes (landslide dynamic and erosion studies) (Tanyaş et al., 2017). In this case, the limitation is the lack of differentiation between landslide sources and depositional areas.

We also evaluate the completeness level of the co-seismic landslide inventory based on the method suggested by Tanyaş and Lombardo (2020). The method proposed a completeness evaluation which returns a Low, Moderate, and High completeness class by essentially addressing two questions:

(i) Are landslides mapped for the entire landslide-affected area?

(ii) Is the mapping resolution of inventory enough to identify small landslides?

Based on these questions, Tanyaş and Lombardo (2020) indicated that at least half the area affected by landslides needs to be examined and also the rollover size should be equal or smaller than 500 m^2 to refer to a "High Completeness" for an EQIL inventory.

Our analyses show that the 0.26 g isoline represents the most likely area affected by EQILs (following Tanyaş and Lombardo, 2019), and in this study we systematically examined 86% of this area by visual interpretation (see Figure 4). Therefore, the majority of the target area was investigated. On the other hand, the rollover value of our inventory (600 m^2) is slightly larger than the threshold (500 m^2) indicated by Tanyaş and Lombardo (2020). This indicates that the completeness index of the 2018 PNG co-seismic landslide inventory is at the transition between “Moderate Completeness” and “High Completeness”.

4.2 Further interpretations

The population of PNG is expanding rapidly and there is ongoing resource development. This leads to the expansion of towns, agricultural land and of the infrastructure supplying them as well as the construction of large industrial processing plants, pipelines and electricity transmission cables. In turn, this results in local and regional deforestation which can also lead to landslides. To facilitate safe and sustainable development, it is essential to assess the risk of landslides in different areas and specifically to understand the main factors controlling that risk. The EQIL inventory resulting from this study allows some preliminary conclusions to be drawn and recommendations for further studies.

The very widespread landslides in February-March 2018 in the PNG Highlands were clearly triggered by the February 25, 2018 M_w 7.5 earthquake and aftershocks. At the same time, both spatial and size distributions of landslides have also shown unique concentrations around some locations. For instance, some of the very large post-seismic landslides have high concentrations near the epicentral area of the both mainshock and three aftershocks (Figure 6). Also, 40% of the mapped landslides occurred in the Sisa and Kerewa volcanics and 36% of the landslides occurred in the Darai Limestone that is exposed over 9% and 34% of the study area (Figure 10), respectively.

Notably, the influence of ground shaking coupled with steep topography and a strong precipitation regime explain the overall distribution of landslides. The Highlands of PNG incorporate over 4000 m of relief, active volcanoes, incised rivers with steep valley walls, heavy rainfall and ongoing active tectonism. All these features lead to the development of landslides triggered by earthquakes. However, this does not rule out the influence of complex interactions between various factors that could have played a significant role in the concentration of the landslides at specific localities.

Complicated interplay between various factors has long been recognized as a valid mechanism triggering large landslides in PNG. In fact, some of the largest landslides in the world occurred in PNG under the influence of seismic, climatic, geologic and structure controls including discontinuity surfaces (Robbins and Petterson, 2015). For instance, the 1985 Bairaman landslide initiated as a rockslide, most likely along bedding planes, and then turned into a debris avalanche covering an area of approximately 1 km^2 and a back scarp up to 200 m high which mobilized approximately 0.18 km^3 of loose material (King et al., 1989). The landslide was triggered by the 1985 M_w=7.2 earthquake that occurred on the island of New Britain (PNG). The 1988 Kaiapit landslide is another example of a landslide triggered by a similar mechanism. It occurred in the Finisterre Range of PNG initiated along a planar discontinuity and evolved into a debris flow that covered an area of 11.4 km^2, with an estimated volume of 2 km^3 (Drechsler et al., 1989; Peart, 1991). The initiation of the Kaiapit landslide was not associated with any specific earthquake or rainfall event and the actual cause behind this gigantic landslide is still not clear. However, the fatigue damage caused by the active tectonics is likely an important factor in triggering the landslides. In fact, Peart (1991) emphasizes the compound effect of various predisposing conditions including seismicity and highly disturbed hillslope materials due to the active tectonics besides the climatic factors.

This study also points out the possible influences of various factors and their interactions. These interactions include the geotechnical characteristics of lithological units in the study area due to the geologic and tectonic history, the possible influence of the earthquakes' energy radiation, the hydrogeological conditions, and their combined effect with geomorphological conditions that will be discussed below.

(i) The Sisa and Kerewa volcanics exist on the flanks of the recently active volcanoes that only occupy ~10% of the study area (Figure 10). The peak of Mount Sisa is at 2689 m and Mount Kerewa at 3635 m, both 1.5-2 kms above the surrounding land. Brown and Robinson (1982) describe the rocks of the volcanic aprons as: "Volcaniclastic, andesitic and basaltic breccia; reworked agglomerate, tuff, minor intercalated volcanically derived conglomerate, sandstone; poorly sorted angular clasts range in size from large boulder to fine silt size; massive, poorly stratified, reworked laharic deposits". Overall, the geotechnical characteristics of Sisa and Kerewa volcanics explain the reason behind the high landslide concentration in these units, which are constituted by weak, soft and unconsolidated materials. Moreover, in the equatorial setting with very high rainfall, these rocks are weathered to very deep levels and are capable of absorbing large amounts of water, making them unstable. Indeed, our work demonstrates that the recently active volcanoes are inherently highly susceptible to landslides when there is strong ground shaking.

(ii) In contrast to the volcanics, the Darai Limestone appears as strong, hard and consolidated rocks. This suggests that it is not an inherently landslide-prone rock and that other factors, such as internal weakening planes or deformation due to external tectonic forces, are more important. The Darai Limestone is >1 km thick in the study area and has 'spectacular tropical karst topography' (Brown and Robinson, 1982) so that water runs-off at surface and through cave systems and is not retained. In the outcrop and on seismic data the Darai Limestone is often very well bedded (Figure 11). Hanani (2012) and Hanani et al. (2016) found that the best seismic reflector in the Darai Limestone was a mid-Darai horizon (Figure 21). The layered vegetation within Darai Limestone cliff faces throughout the fold belt (Figure 21a), and the strong reflectors within seismic data (Figure 21b) indicate good layering and potential planes of weakness perhaps with local shales or even coals. Our analysis suggests that where sub-horizontal, the limestone is mostly stable even where it forms steep hillslopes (Figure 9d). In contrast, where the limestone dips steeply it is much more susceptible to landslides along these weak internal bedding planes. Such steep dips can be seen in the Darai Limestone within Hegigio Gorge, along the Tagari River, where enormous landslides occurred during the PNG mainshock (e.g., Figure 9f). Further along the Tagari River to the northwest, the limestone plunges into the sub-surface and seismic data reveal its steep dipping sub-surface geometry (Figure 11). On the other hand, the Darai Limestone has an active tectonic history of folding (ductile deformation) followed by thrust faulting (brittle deformation) as shown in the seismic section in Figure 11d (e.g., Hill et al., 2015). Such an active tectonic history would have caused not only steeply-dipping bedding planes introducing high landslide susceptibility but also fatigue damage and weakening of the rock units over geologic times.

Regrettably, we could not assess the role of either tectonic deformation or structural features in the multivariate analyses because of the lack of proxies/layers representing these features for the entire study area.

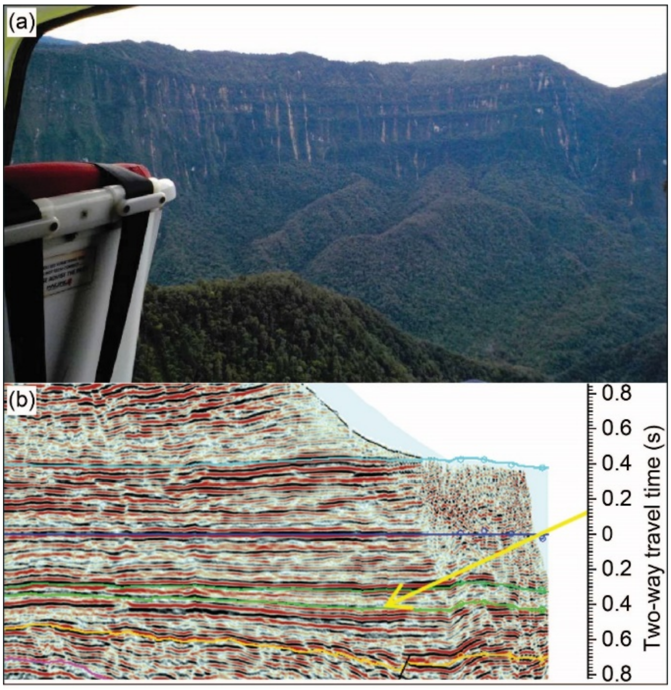

Figure 21. Sub-horizontal bedding planes of Darai Limestone. Panel (a) shows a cliff formed by the bedding planes of Darai Limestone in Tingi valley and (b) indicates seismic reflectors in the Darai Limestone in the Juha area from Hanani (2012). The yellow arrow points to the base of the Darai. The top of the Darai is the light blue horizon. The seismic data are flattened on the strong mid-Darai reflector in dark blue. Photo courtesy of Papuan Oil Search.

(iii) Disturbed hillslope materials is another factor that could contribute to the landslides distribution in the area. Our image analysis showed an example of such distributed hillslope materials after the mainshock in Figure 12. It is reasonable to assume that the earthquake history in the study area may have produced abundant similar weakness planes over geological timescales (see Figure 12b and 12c), but they are difficult to identify beneath the thick vegetation cover. If this hypothesis is reasonable, then it is also reasonable to assume that the weakened rocks highlighted in Figures 12b and 12c may be the next candidate to fail, either by mechanical processes such as ground motion and/or precipitation.

(iv) The influence of rainfalls has been considered as the most common triggering factor of landslides in PNG (Greenbaum et al., 1995; Robbins and Petterson, 2015). In this context, the 2018 PNG landslide events is not an exceptional.

For the co-seismic landslides, our analysis shows that the area had the highest cumulative 15-days antecedent precipitation among other EQILs reported in the literature (Figure 15). Therefore, the significant rainfall amount before the mainshock may have changed the hydrogeological conditions of the landslides affected area indirectly due to complex structural and geologic controls leading to the higher water table and increased pore water pressure. As a result, this may have elevated the landslide susceptibility just before the mainshock.

For the post-seismic case, the rainfall may have played a slightly different role. Our findings showed that the post-seismic landslides occurred on less-steep slopes compared to their co-seismic counterparts (Figure 10) and as shown in Figures 11 and 12, concentrated at the boundaries between the lithological units. One likely explanation for this observation is associated with the weakening effect of the mainshock and also the amalgamation of the discontinuity surfaces generated by the mainshock in the post-seismic phase. However, we need to stress that post-seismic landslides mostly occurred in volcanic rocks (Figure 10) that are less strong and therefore much less likely to form steep slopes in the first place. The fact that some of the largest mapped landslides are post-seismic and were concentrated at the boundary between different lithological units needs further attention here.

While the accumulated stress of the PGAs from the mainshock and the aftershock have partially explained the concentration of those very large post-seismic landslides, the concentration of the post-seismic landslide population at the boundary between different lithologic units could potentially be due to the combined effect of local site conditions and high rainfall precipitation besides the accumulated stress. For instance, Figure 11a shows post-seismic landslides triggered at the boundary between the Wongop sandstone and Sisa volcanic. It is worth noting that these are some of the largest landslides we mapped in this study. In this case, to better understand the local site conditions, we need to take into account the high precipitation events after the mainshock and the possibility of differential permeability between the Wongop sandstone (with high permeability) and Sisa volcanic (with relatively lower permeability due to the intrinsic nature of the composite of such weathered volcanics). One possible scenario could be that the Sisa Volcanics have preserved or absorbed the rainfall water (becoming softer), which led to a higher water table relative to the surrounding lithological units. The local reduction in the shear wave velocity due to the increased water content may have led to local seismic site amplification. This may have locally amplified the seismic signals of the aftershocks and led to a differential propagation pattern in terms of amplitude and frequency content across the lithologic boundary (Ikeda and Tsuji, 2016), approximately around 1 second (e.g., Mayoral et al., 2019).

(v) Taking aside the seismic amplification that might have occurred along geological boundaries, topographic amplification can also be an added factor due to the high topography of the study area within the PNG Fold Belt. Our results show a high concentration of landslides at the flanks of mountains (e.g., Mount Sisa and Mount Kerewa covered with volcanics; Figures 9 and 11), where seismic waves could be expected to be amplified near the ridge crests (e.g., Jafarzadeh et al., 2015; Meunier et al., 2008; Rizzitano et al., 2014). Moreover, the vertical variation of the geological units over steep hillslopes due to complex tectonic history and eruption cycles (e.g., at the Tagari Valley where Darai Limestone exists) could lead to extra amplification of seismic waves (e.g., Ikeda and Tsuji, 2016; Mayoral et al., 2019; Figure 1e).

We speculate that these factors could have all together played a role in the concentration of landslides at specific localities. However, further local investigations are needed to support or reject these interpretations which stays as an open question for future studies.

5 Conclusion

In this paper, we explored a unique site where rainfall and a seismic swarm contextually affected the landscape over a short period of time. We mapped not only the landslides triggered by the mainshock of the 2018 PNG seismic swarm (i.e., co-seismic landslides) but also those most likely triggered in a 8-day period between February 27 and March 7 by the compound effect of both subsequent aftershocks and/or rainfall events (i.e., post-seismic landslides).

Analyses performed for the co-seismic landslides returned a landslide-event magnitude second only to the disastrous Wenchuan case.

We performed descriptive analyses as well as bivariate and multivariate analyses to explain the influence of various factors that can be interchangeably and/or simultaneously controlled the spatial and size distributions of landslides. Contribution of those factors are spatially diverse for both co- and post- seismic landslides. And yet, overall, six main factors can be listed as significant:

- the intensity of seismic shaking,
- steep topography
- high rainfall
- geological units and their geotechnical characteristics,
- structural features (e.g., bedding planes) and,
- active tectonics weakening hillslope and causing fatigue damage.

Approximately 90% of the co-seismic landslides occurred within 20 km wide buffer zone where PGA is larger than 0.5 g and triggered large landslides up to the size of ~3 km^2. Intense ground shaking also appeared as a significant factor controlling spatial and size distribution of post-seismic landslides. The post-seismic landslides, these appear to be extremely large, even when compared to their counterparts associated with earthquakes such as Wenchuan, Gorkha and Haiti. To understand the reason behind these large landslides, we examined the role of aftershocks. In turn, for the first time in the literature we statistically estimated the cumulated effect of aftershocks on the post-seismic landslide size distribution.

Overall, majority of the whole landslide population occurred on steep hillslopes and only ~14% of them occurred on hillslopes less steeper than 20°. However, large landslides also occurred on those relatively less steep hillslopes depending on other factors such as precipitation and geology.

We showed that among all EQIL inventories, the area affected by the 2018 PNG swarm is the site with the largest exposure to rainfall in terms of 15-day antecedent precipitation. In fact, the precipitation regime prior to the mainshock appears to have played a relevant role in the spatial distribution of co-seismic slope failures.

Our findings also showed that the majority of the landslides occurred in the volcanic beds on the flanks of the modern and active Mount Kerewa and Mount Sisa volcanoes, although these volcanic units cover a very small part of the study area. These units constitute weaker and unconsolidated material, which is also highly weathered. Therefore, geotechnical features of the volcanics reveal the weak and unstable characteristics of these units. The second largest number of EQILs occurred in the Darai Limestone, which covers most of the study area. Our observation showed that the most common failure planes within the limestones were related to bedding. However, the limestones are not as susceptible to failure as the volcanic units unless they are deformed and tilted in a way that the bedding planes become mechanically unstable. Tectonic deformation and the associated fatigue damage clearly played a key role in initiating catastrophic landslides within the limestones.

Overall, the complexity of the geological, tectonic, climatic settings and local seismic site amplifications caused by different water holding capacity of adjacent geological units may be the cause of this unique sequence of landslide occurrences. Direct observations of tension cracks imply that pre-existing weakness surfaces have promoted widespread slope instabilities certainly for the post-seismic landslide and likely for the co-seismic ones.

In this complex system, further research should be conducted to gain insight on the dominant processes controlling landslides in this area. A better understanding can be the key to reduce the potential risk in a location where the second largest landslide event ever recorded took place.

Acknowledgments

The authors wish to thank Papuan Oil Search, ExxonMobil and Santos for permission to publish the seismic section and photos taken from the site. The inventories we mapped for this study will be shared through the Supplementary Materials upon acceptance of this manuscript.

References

Abers, G., McCaffrey, R., 1988. Active deformation in the New Guinea fold-and-thrust belt: Seismological evidence for strike-slip faulting and basement-involved thrusting. J. Geophys. Res. Solid Earth 93, 13332–13354. https://doi.org/https://doi.org/10.1029/JB093iB11p13332

Allstadt, K.E., Thompson, E.M., Wald, D.J., Hamburger, M.W., Godt, J.W., Knudsen, K.L., Jibson, R.W., Jessee, M.A., Zhu, J., Hearne, M., Baise, L.G., Tanyas, H., Marano, K.D., 2016. USGS approach to real-time estimation of earthquake-triggered ground failure - Results of 2015 workshop, Open-File Report. Reston, VA. https://doi.org/10.3133/ofr20161044

Alvioli, M., Marchesini, I., Reichenbach, P., Rossi, M., Ardizzone, F., Fiorucci, F., Guzzetti, F., 2016. Automatic delineation of geomorphological slope units with r.slopeunits v1.0 and their optimization for landslide susceptibility modeling. Geosci. Model Dev. 9, 3975–3991. https://doi.org/10.5194/gmd-9-3975-2016

Ambrosi, C., Crosta, G.B., 2006. Large sackung along major tectonic features in the Central Italian Alps. Eng. Geol. 83, 183–200. https://doi.org/https://doi.org/10.1016/j.enggeo.2005.06.031

Brown, C.M., Robinson, G.P., 1982. Kutubu 1:250 000 geological series explanatory notes sheet SB/54-12, geological survey of Papua New Guinea. Port Moresby: PNG Department of Minerals and Energy.

Chigira, M., Wang, W.-N., Furuya, T., Kamai, T., 2003. Geological causes and geomorphological precursors of the Tsaoling landslide triggered by the 1999 Chi-Chi earthquake, Taiwan. Eng. Geol. 68, 259–273. https://doi.org/https://doi.org/10.1016/S0013-7952(02)00232-6

Chigira, M., Yagi, H., 2006. Geological and geomorphological characteristics of landslides triggered by the 2004 Mid Niigta prefecture earthquake in Japan. Eng. Geol. 82, 202–221. https://doi.org/10.1016/j.enggeo.2005.10.006

Chong, J., Huang, M., 2020. Refining the 2018 Mw 7.5 Papua New Guinea Earthquake Fault-Slip Model Using Subpixel Offset. Bull. Seismol. Soc. Am. 111, 1032–1042. https://doi.org/10.1785/0120200250

CIA, 2018. The World Factbook 2018. URL https://www.cia.gov/the-world-factbook (accessed 7.13.21).

Dai, F.C., Tu, X.B., Xu, C., Gong, Q.M., Yao, X., 2011. Rock avalanches triggered by oblique-thrusting during the 12 May 2008 Ms 8.0 Wenchuan earthquake, China. Geomorphology 132, 300–318. https://doi.org/https://doi.org/10.1016/j.geomorph.2011.05.016

Davies, H., 1983. Wabag 1:250 000 Geological Series Explanatory Notes Sheet SB/54-8, Geological Survey of Papua New Guinea. PNG Department of Minerals and Energy, Port Moresby.

Davies, H., Norvick, M., 1974. Blucher range 1:250 000 geological series explanatory notes sheet SB/54-07. Geological survey of Papua New Guinea. Port Moresby: PNG Department of Minerals and Energy.

Drechsler, M., Ripper, I., Rooke, E., Warren, E., 1989. The Kaiapit landslide, Papua New Guinea, in: Proceedings of the International Conference on Engineering Geology in Tropical Terrains, Malaysia, June 1989, 1-10.

Fan, X., Scaringi, G., Korup, O., West, A.J., van Westen, C.J., Tanyas, H., Hovius, N., Hales, T.C., Jibson, R.W., Allstadt, K.E., Zhang, L., Evans, S.G., Xu, C., Li, G., Pei, X., Xu, Q., Huang, R., 2019. Earthquake-Induced Chains of Geologic Hazards: Patterns, Mechanisms, and Impacts. Rev. Geophys. 57. https://doi.org/10.1029/2018RG000626

Gallen, S.F., Clark, M.K., Godt, J.W., Roback, K., Niemi, N.A., 2017. Application and evaluation of a rapid response earthquake-triggered landslide model to the 25 April 2015 Mw 7.8 Gorkha earthquake, Nepal. Tectonophysics 714–715, 173–187. https://doi.org/10.1016/j.tecto.2016.10.031

Gorum, T., Fan, X., van Westen, C.J., Huang, R.Q., Xu, Q., Tang, C., Wang, G., 2011. Distribution pattern of earthquake-induced landslides triggered by the 12 May 2008 Wenchuan earthquake. Geomorphology 133, 152–167. https://doi.org/10.1016/j.geomorph.2010.12.030

Gorum, T., Korup, O., van Westen, C.J., van der Meijde, M., Xu, C., van der Meer, F.D., 2014. Why so few? Landslides triggered by the 2002 Denali earthquake, Alaska. Quat. Sci. Rev. 95, 80–94. https://doi.org/10.1016/j.quascirev.2014.04.032

Greenbaum, D., Tutton, M., Bowker, M.R., Browne, T.J., Buleka, J., Greally, K.B., Kuna, G., McDonald, A.J.W., Marsh, S.H., Northmore, K.H., others, 1995. Rapid methods of landslide hazard mapping: Papua New Guinea case study.

Hanani, A., 2012. The Geology and Structural Style of the Juha Gas Field, Papua New Guinea. Honours Thesis (unpublish). The University of New South Wales, Sydney.

Hanani, A., Lennox, P., Hill, K., 2016. The geology and structural style of the Juha gas field, Papua New Guinea. ASEG Ext. Abstr. 2016, 1–7.

Harp, E.L., Jibson, R.W., 1995. Inventory of landslides triggered by the 1994 Northridge, California earthquake, Open-File Report. https://doi.org/10.3133/ofr95213

Harp, E.L., Jibson, R.W., Schmitt, R.G., 2016. Map of landslides triggered by the January 12, 2010, Haiti earthquake. https://doi.org/10.3133/sim3353

Hill, K., Wightman, R., Munro, L., 2015. Structural style in the Eastern Papuan Fold Belt, from wells, seismic, maps and modelling.

Hill, K.C., Hall, R., 2003. Mesozoic-Cenozoic evolution of Australia's New Guinea margin in a west Pacific context. Spec. Pap. Soc. Am. 265–290.

Hill, K.C., Kendrick, R.D., Crowhurst, P. V, Gow, P.A., 2002. Copper-gold mineralisation in New Guinea: Tectonics, lineaments, thermochronology and structure. Aust. J. Earth Sci. 49, 737–752.

Hill, K.C., Medd, D., Darvall, P., 1990. Structure, stratigraphy, geochemistry and hydrocarbons in the Kagua-Kubor area, Papua New Guinea. Papua New Guinea (PNG) Petroleum Convention Proceedings.

Hill, K.C., Raza, A., 1999. Arc-continent collision in Papua Guinea: Constraints from fission track thermochronology. Tectonics 18, 950–966.

Hosmer, D.W., Lemeshow, S., 2000. Applied Logistic Regression. John Wiley & Sons. New York.

Huffman, G., Stocker, E.F., T, B.D., Nelkin, E.J., Tan, J., 2019. GPM IMERG Final Precipitation L3 1 day 0.1 degree x 0.1 degree V06. Ed. by Andrey Savtchenko,

Greenbelt, MD, Goddard Earth Sci. Data Inf. Serv. Cent. (GES DISC).
Ikeda, T., Tsuji, T., 2016. Surface wave attenuation in the shallow subsurface from multichannel–multishot seismic data: a new approach for detecting fractures and lithological discontinuities. Earth, Planets Sp. 68, 111. https://doi.org/10.1186/s40623-016-0487-0
Jafarzadeh, F., Shahrabi, M.M., Jahromi, H.F., 2015. On the role of topographic amplification in seismic slope instabilities. J. Rock Mech. Geotech. Eng. 7, 163–170.
Jibson, R.W., 2007. Regression models for estimating coseismic landslide displacement. Eng. Geol. 91, 209–218. https://doi.org/10.1016/j.enggeo.2007.01.013
Jibson, R.W., Harp, E.L., Michael, J.A., 2000. A method for producing digital probabilistic seismic landslide hazard maps. Eng. Geol. 58, 271–289. https://doi.org/10.1016/S0013-7952(00)00039-9
Kaynia, A.M., Skurtveit, E., Saygili, G., 2011. Real-time mapping of earthquake-induced landslides. Bull. Earthq. Eng. 9, 955–973. https://doi.org/10.1007/s10518-010-9234-2
Keefer, D.K., 2000. Statiscal analysis of an earthquake-induced landslide distribution - The 1989 Loma Prieta, California event. Eng. Geol. 58, 231–249. https://doi.org/10.1016/S0013-7952(00)00037-5
King, J., Loveday, I., Schuster, R.L., 1989. The 1985 Bairaman landslide dam and resulting debris flow, Papua New Guinea. Q. J. Eng. Geol. Hydrogeol. 22, 257–270. https://doi.org/10.1144/GSL.QJEG.1989.022.04.02
Korup, O., 2004. Geomorphic implications of fault zone weakening: Slope instability along the Alpine Fault, South Westland to Fiordland. New Zeal. J. Geol. Geophys. 47, 257–267. https://doi.org/10.1080/00288306.2004.9515052
Kritikos, T., Robinson, T.R., Davies, T.R.H., 2015. Regional coseismic landslide hazard assessment without historical landslide inventories: A new approach. J. Geophys. Res. Earth Surf. 120, 711–729. https://doi.org/10.1002/2014JF003224
Leroueil, S., 2001. Natural slopes and cuts: Movement and failure mechanisms. Geotechnique 51, 197–243. https://doi.org/10.1680/geot.2001.51.3.197
Liao, H.W., Lee, C.T., 2000. Liao, H.W. and Lee, C.T. (2000) Landsides triggered by the Chi-Chi Earthquake, Proceedings of the 21 1, 383–388.
Ling, S., Chigira, M., 2020. Characteristics and triggers of earthquake-induced landslides of pyroclastic fall deposits: An example from Hachinohe during the 1968 M7.9 tokachi-Oki earthquake, Japan. Eng. Geol. 264, 105301. https://doi.org/https://doi.org/10.1016/j.enggeo.2019.105301
Lombardo, L., Tanyas, H., Huser, R., Guzzetti, F., Camilo, D.C., 2021. Landslide size matters: a new spatial predictive paradigm.
Mahoney, L., Hill, K., McLaren, S., Hanani, A., 2017. Complex fold and thrust belt structural styles: Examples from the Greater Juha area of the Papuan Fold and Thrust Belt, Papua New Guinea. J. Struct. Geol. 100, 98–119. https://doi.org/https://doi.org/10.1016/j.jsg.2017.05.010
Mahoney, L., Mclaren, S., Hill, K., Kohn, B., Gallagher, K., Norvick, M., 2019. Late Cretaceous to Oligocene burial and collision in western Papua New Guinea: Indications from low-temperature thermochronology and thermal modelling. Tectonophysics 752, 81–112.
Mahoney, L., Stanaway, R., McLaren, S., Hill, K., Bergman, E., 2021. The 2018 Mw 7.5 Highlands Earthquake in Papua New Guinea: Implications for Structural Style in an Active Fold and Thrust Belt. Tectonics 40, e2020TC006667. https://doi.org/https://doi.org/10.1029/2020TC006667
Malamud, B.D., Turcotte, D.L., Guzzetti, F., Reichenbach, P., 2004. Landslide inventories and their statistical properties. Earth Surf. Process. Landforms 29, 687–711. https://doi.org/10.1002/esp.1064
Massey, C., Townsend, D., Rathje, E., Allstadt, K.E., Lukovic, B., Kaneko, Y., Bradley, B., Wartman, J., Jibson, R.W., Petley, D.N., Horspool, N., Hamling, I., Carey, J., Cox, S., Davidson, J., Dellow, S., Godt, J.W., Holden, C., Jones, K., Kaiser, A., Little, M., Lyndsell, B., McColl, S., Morgenstern, R., Rengers, F.K., Rhoades, D., Rosser, B.,

Strong, D., Singeisen, C., Villeneuve, M., 2018. Landslides triggered by the 14 November 2016 Mw 7.8 Kaikōura earthquake, New Zealand. Bull. Seismol. Soc. Am. 108, 1630–1648. https://doi.org/10.1785/0120170305

Mayoral, J.M., De la Rosa, D., Tepalcapa, S., 2019. Topographic effects during the September 19, 2017 Mexico city earthquake. Soil Dyn. Earthq. Eng. 125, 105732. https://doi.org/https://doi.org/10.1016/j.soildyn.2019.105732

McBride, J.L., Haylock, M.R., Nicholls, N., 2003. Relationships between the Maritime Continent Heat Source and the El Niño–Southern Oscillation Phenomenon. J. Clim. 16, 2905–2914. https://doi.org/10.1175/1520-0442(2003)016<2905:RBTMCH>2.0.CO;2

Meunier, P., Hovius, N., Haines, A.J., 2007. Regional patterns of earthquake-triggered landslides and their relation to ground motion. Geophys. Res. Lett. 34, 1–5. https://doi.org/10.1029/2007GL031337

Meunier, P., Hovius, N., Haines, J.A., 2008. Topographic site effects and the location of earthquake induced landslides. Earth Planet. Sci. Lett. 275, 221–232. https://doi.org/10.1016/j.epsl.2008.07.020

NASA JPL, 2013. NASA Shuttle Radar Topography Mission United States 1 Arc Second. NASA EOSDIS Land Processes DAAC, USGS Earth Resources Observation and Science (EROS) Center, Sioux Falls, South Dakota https://lpdaac.usgs.gov, Accessed date: 1 December 2019. [WWW Document].

Nowicki Jessee, M.A., Hamburger, M.W., Allstadt, K., Wald, D.J., Robeson, S.M., Tanyas, H., Hearne, M., Thompson, E.M., 2018. A Global Empirical Model for Near-Real-Time Assessment of Seismically Induced Landslides. J. Geophys. Res. Earth Surf. 123, 1835–1859. https://doi.org/10.1029/2017JF004494

Nowicki, M.A., Wald, D.J., Hamburger, M.W., Hearne, M., Thompson, E.M., 2014. Development of a globally applicable model for near real-time prediction of seismically induced landslides. Eng. Geol. 173, 54–65. https://doi.org/10.1016/j.enggeo.2014.02.002

Pain, C.F., 1972. Characteristics and geomorphic effects of earthquake-initiated landslides in the adelbert range, Papua New Guinea. Eng. Geol. 6, 261–274. https://doi.org/https://doi.org/10.1016/0013-7952(72)90011-7

Parker, R.N., Rosser, N.J., Hales, T.C., 2017. Spatial prediction of earthquake-induced landslide probability. Nat. Hazards Earth Syst. Sci. Discuss. 2017, 1–29. https://doi.org/10.5194/nhess-2017-193

Peart, M., 1991. The Kaiapit Landslide: events and mechanisms. Q. J. Eng. Geol. Hydrogeol. 24, 399–411. https://doi.org/10.1144/GSL.QJEG.1991.024.04.07

Pegler, G., Das, S., Woodhouse, J.H., 1995. A seismological study of the eastern New Guinea and the western Solomon Sea regions and its tectonic implications. Geophys. J. Int. 122, 961–981.

Penna, I.M., Abellán, A., Humair, F., Jaboyedoff, M., Daicz, S., Fauqué, L., 2017. The role of tectonic deformation on rock avalanche occurrence in the Pampeanas Ranges, Argentina. Geomorphology 289, 18–26. https://doi.org/https://doi.org/10.1016/j.geomorph.2016.07.006

Perrone, A., Vassallo, R., Lapenna, V., Di Maio, C., 2008. Pore water pressures and slope stability: a joint geophysical and geotechnical analysis. J. Geophys. Eng. 5, 323–337. https://doi.org/10.1088/1742-2132/5/3/008

Planet Team, 2017. Planet Application Program Interface: In Space for Life on Earth. San Francisco, CA. https://api.planet.com [WWW Document].

Rizzitano, S., Cascone, E., Biondi, G., 2014. Coupling of topographic and stratigraphic effects on seismic response of slopes through 2D linear and equivalent linear analyses. Soil Dyn. Earthq. Eng. 67, 66–84. https://doi.org/https://doi.org/10.1016/j.soildyn.2014.09.003

Roback, K., Clark, M.K., West, A.J., Zekkos, D., Li, G., Gallen, S.F., Chamlagain, D., Godt, J.W., 2018. The size, distribution, and mobility of landslides caused by the 2015 Mw7.8 Gorkha earthquake, Nepal. Geomorphology 301, 121–138. https://doi.org/10.1016/j.geomorph.2017.01.030

Robbins, J.C., Petterson, M.G., 2015. Landslide inventory development in a data sparse region: spatial and temporal characteristics of landslides in Papua New Guinea. Nat. Hazards Earth Syst. Sci. Discuss. 2015, 4871–4917. https://doi.org/10.5194/nhessd-3-4871-2015

Robbins, J.C., Petterson, M.G., Mylne, K., Espi, J.O., 2013. Tumbi Landslide, Papua New Guinea: rainfall induced? Landslides 10, 673–684. https://doi.org/10.1007/s10346-013-0422-4

Robertson, A.W., Moron, V., Qian, J.-H., Chang, C.-P., Tangang, F., Aldrian, E., Koh, T.Y., Liew, J., 2011. The maritime continent monsoon, in: The Global Monsoon System, World Scientific Series on Asia-Pacific Weather and Climate. WORLD SCIENTIFIC, pp. 85–98. https://doi.org/doi:10.1142/9789814343411_0006

Robinson, T.R., Rosser, N.J., Densmore, A.L., Williams, J.G., Kincey, M.E., Benjamin, J., Bell, H.J.A., 2017. Rapid post-earthquake modelling of coseismic landslide intensity and distribution for emergency response decision support. Nat. Hazards Earth Syst. Sci. 17, 1521–1540. https://doi.org/10.5194/nhess-17-1521-2017

Saade, A., Abou-Jaoude, G., Wartman, J., 2016. Regional-scale co-seismic landslide assessment using limit equilibrium analysis. Eng. Geol. 204, 53–64. https://doi.org/10.1016/j.enggeo.2016.02.004

Sassa, K., Fukuoka, H., Wang, F., Wang, G., 2007. Landslides Induced by a Combined Effect of Earthquake and Rainfall, in: Sassa, K., Fukuoka, H., Wang, F., Wang, G. (Eds.), Progress in Landslide Science. Springer Berlin Heidelberg, Berlin, Heidelberg, pp. 193–207. https://doi.org/10.1007/978-3-540-70965-7_14

Scheibner, E., 1974. Fossil fracture zones (transform faults), segmentation and correlation problems in the Tasman Fold Belt System, in: The Tasman Geosyncline–A Symposium in Honour of Professor Dorothy Hill, Queensland Division Geological Society of Australia, Brisbane. pp. 65–96.

Schmitt, R.G., Tanyas, H., Nowicki Jessee, M.A., Zhu, J., Biegel, K.M., Allstadt, K.E., Jibson, R.W., Thompson, E.M., van Westen, C.J., Sato, H.P., Wald, D.J., Godt, J.W., Gorum, T., Xu, C., Rathje, E.M., Knudsen, K.L., 2017. An open repository of earthquake-triggered ground-failure inventories, Data Series. Reston, VA. https://doi.org/10.3133/ds1064

Simonett, D.S., 1967. Landslide distribution and earthquakes in the Bavani and Torricelli Mountains, New Guinea. Landf. Stud. from Aust. New Guinea 64–84.

Smith, I., Moise, A., Inape, K., Murphy, B., Colman, R., Power, S., Chung, C., 2013. ENSO-related rainfall changes over the New Guinea region. J. Geophys. Res. Atmos. 118, 10,610-665,675. https://doi.org/https://doi.org/10.1002/jgrd.50818

Smith, I.N., Moise, A.F., Colman, R.A., 2012. Large-scale circulation features in the tropical western Pacific and their representation in climate models. J. Geophys. Res. Atmos. 117. https://doi.org/https://doi.org/10.1029/2011JD016667

Song, J., Rodriguez-Marek, A., Feng, T., Ji, J., 2021. A generalized seismic sliding model of slopes with multiple slip surfaces. Earthq. Eng. Struct. Dyn. n/a. https://doi.org/https://doi.org/10.1002/eqe.3462

Stanley, G.A.., 1935. Preliminary notes on the recent earthquake in New Guinea. Aust. Geogr. 2, 8–15. https://doi.org/10.1080/00049183508702151

Stead, D., Wolter, A., 2015. A critical review of rock slope failure mechanisms: The importance of structural geology. J. Struct. Geol. 74, 1–23. https://doi.org/https://doi.org/10.1016/j.jsg.2015.02.002

Steger, S., Brenning, A., Bell, R., Petschko, H., Glade, T., 2016. Exploring discrepancies between quantitative validation results and the geomorphic plausibility of statistical landslide susceptibility maps. Geomorphology 262, 8–23. https://doi.org/https://doi.org/10.1016/j.geomorph.2016.03.015

Steger, S., Mair, V., Kofler, C., Pittore, M., Zebisch, M., Schneiderbauer, S., 2021. Correlation does not imply geomorphic causation in data-driven landslide susceptibility modelling – Benefits of exploring landslide data collection effects. Sci. Total Environ. 776, 145935. https://doi.org/https://doi.org/10.1016/j.scitotenv.2021.145935

Tanyaş, H., Allstadt, K.E., van Westen, C.J., 2018. An updated method for estimating landslide-event magnitude. Earth Surf. Process. Landforms. https://doi.org/10.1002/esp.4359

Tanyaş, H., Kirschbaum, D., Lombardo, L., 2021. Capturing the footprints of ground motion in the spatial distribution of rainfall-induced landslides. Bull. Eng. Geol. Environ. https://doi.org/10.1007/s10064-021-02238-x

Tanyaş, H., Lombardo, L., 2020. Completeness Index for Earthquake-Induced Landslide Inventories. Eng. Geol. 264, 105331. https://doi.org/https://doi.org/10.1016/j.enggeo.2019.105331

Tanyaş, H., Lombardo, L., 2019. Variation in landslide-affected area under the control of ground motion and topography. Eng. Geol. 260. https://doi.org/10.1016/j.enggeo.2019.105229

Tanyaş, Hakan, Rossi, M., Alvioli, M., van Westen, C.J., Marchesini, I., 2019. A global slope unit-based method for the near real-time prediction of earthquake-induced landslides. Geomorphology 327, 126–146. https://doi.org/10.1016/j.geomorph.2018.10.022

Tanyaş, H., Rossi, M., Alvioli, M., van Westen, C.J., Marchesini, I., 2019a. A global slope unit-based method for the near real-time prediction of earthquake-induced landslides. Geomorphology 327. https://doi.org/10.1016/j.geomorph.2018.10.022

Tanyaş, H., van Westen, C.J., Allstadt, K.E., Anna Nowicki Jessee, M., Görüm, T., Jibson, R.W., Godt, J.W., Sato, H.P., Schmitt, R.G., Marc, O., Hovius, N., 2017. Presentation and Analysis of a Worldwide Database of Earthquake-Induced Landslide Inventories. J. Geophys. Res. Earth Surf. 122. https://doi.org/10.1002/2017JF004236

Tanyaş, H., van Westen, C.J., Allstadt, K.E., Jibson, R.W., 2019b. Factors controlling landslide frequency–area distributions. Earth Surf. Process. Landforms 44. https://doi.org/10.1002/esp.4543

Tanyaş, H., van Westen, C.J., Persello, C., Alvioli, M., 2019c. Rapid prediction of the magnitude scale of landslide events triggered by an earthquake. Landslides 16. https://doi.org/10.1007/s10346-019-01136-4

USGS, 2021. United States geological survey earthquake portal. Earthquake Hazards Program [WWW Document]. URL https://www.usgs.gov/%0Anatural-hazards/earthquake-hazards/earthquakes (accessed 4.27.21).

Wallace, L.M., Stevens, C., Silver, E., McCaffrey, R., Loratung, W., Hasiata, S., Stanaway, R., Curley, R., Rosa, R., Taugaloidi, J., 2004. GPS and seismological constraints on active tectonics and arc-continent collision in Papua New Guinea: Implications for mechanics of microplate rotations in a plate boundary zone. J. Geophys. Res. Solid Earth 109. https://doi.org/https://doi.org/10.1029/2003JB002481

Wang, F., Fan, X., Yunus, A.P., Siva Subramanian, S., Alonso-Rodriguez, A., Dai, L., Xu, Q., Huang, R., 2019. Coseismic landslides triggered by the 2018 Hokkaido, Japan (Mw 6.6), earthquake: spatial distribution, controlling factors, and possible failure mechanism. Landslides 16, 1551–1566. https://doi.org/10.1007/s10346-019-01187-7

Wang, S., Xu, C., Li, Z., Wen, Y., Song, C., 2020. The 2018 Mw 7.5 Papua New Guinea Earthquake: A Possible Complex Multiple Faults Failure Event With Deep-Seated Reverse Faulting. Earth Sp. Sci. 7, e2019EA000966. https://doi.org/https://doi.org/10.1029/2019EA000966

Wasowski, J., Keefer, D.K., Lee, C.T., 2011. Toward the next generation of research on earthquake-induced landslides: Current issues and future challenges. Eng. Geol. 122, 1–8. https://doi.org/10.1016/j.enggeo.2011.06.001

WHO, 2018. Papua New Guinea Earthquake Situation Report No. 2 28 MARCH 2018.

WMO, 2018. WMO El Niño/La Niña Update September 2018.

Worden, C.B., Wald, D.J., 2016. ShakeMap manual online: Technical manual, user's guide, and software guide. US Geol. Surv. https//doi. org/10.5066/F7D21VPQ.

Xu, C., Xu, X., Yao, X., Dai, F., 2014. Three (nearly) complete inventories of landslides triggered by the May 12, 2008 Wenchuan Mw 7.9 earthquake of China and their spatial distribution statistical analysis. Landslides 11, 441–461. https://doi.org/10.1007/s10346-013-0404-6

1275